UNIVERSITY OF CALIFORNIA
RIVERSIDE

The Development of Optical Coherence Tomography to Study Optical Changes of Cortical Tissue During Seizures

A Dissertation submitted in partial satisfaction
of the requirements for the degree of

Doctor of Philosophy

in

Bioengineering

by

Melissa Marion Eberle

August 2015

Dissertation Committee:
Dr. B. Hyle Park, Chairperson
Dr. Devin K. Binder
Dr. Todd A. Fiacco

The Dissertation of Melissa Marion Eberle is approved:

_____

_____

_____

Committee Chairperson

University of California, Riverside

ACKNOWLEDGMENTS

It truly takes a village to obtain a PhD and I have had the most amazing support throughout this process. I could not have done it without them!

First, I would like to express my deepest gratitude to my advisor, Dr. Hyle Park, for being an incredible mentor and friend over the past five years. This work would not have been possible without his guidance and support. Thank you for the endless manuscript edits and figure making, for the hours of presenting practice, and for patiently teaching me and answering all of my random questions. Thank you for your dedication to helping all of us succeed. Thank you for the laughs, I am honored to have had to opportunity to work in your lab.

I would like to especially thank my dissertation committee members, Dr. Devin Binder and Dr. Todd Fiacco. This project has been in collaboration with Dr. Binder and he has provided continual guidance and insight through his expertise in neuroscience and clinical neurosurgery. His support and feedback over the years is greatly appreciated. Dr. Fiacco, who also served on my candidacy committee, has provided valuable biological insight to my optical results and I am grateful for his guidance throughout the completion of this project.

I would also like to thank all the other faculty members that have supported me and contributed to my success. I would like to thank Dr. Kaustabh Ghosh and Dr. Victor Rodgers, who both served on my candidacy committee. Thank you to Dr. Bir Bhanu and the faculty advisors of the National Science Foundation Integrative Graduate Education, Research and Training (IGERT) program in Video Bioinformatics for accepting me into

this training program that provided me with two years of financial support. This program was a great learning experience and the interdisciplinary education and training of the program will continue to serve me throughout my career.

I want to give a huge thank you for all the amazing support I have received from the Neuroscience and Optical Imaging Research group at UCR! This has been the best group of people to work with a person could ask for. Dr. Carissa Rodriguez aka (Crey) has been the most amazing friend, lab mate, partner-in-crime, and colleague during my five years here. I don't think this would have been possible without her sitting across from me every day. I am sorry I bugged you constantly, but thank you for putting up with me, for yelling at Matlab with me, for coffee and snack trips, and for making this craziness more fun than I think it's supposed to be. I want to thank Dr. Yan Wang, Dr. Shahid Islam, and Christian Oh for establishing the lab and helping me in the beginning and throughout this process. Thank you to Dr. Michael Oliveira, Dr. Rezuanul Haque, Koji Hirota, Masum Hasan, Minh Tong and Danielle Ornelas for their help and support during my time here.

Additionally, I would like to acknowledge the members of our collaborating labs. From Dr. Binder's lab: Jenny Szu and Mike Hsu for assisting with all of our *in vivo* experiments. Thank you for having the patience, expertise and foresight to make the experiments a success. Your help has been invaluable and has made this project possible. From Dr. Maxim Bazhenov's lab: Oscar Gonzalez and Tim Myers for assisting with the *in vitro* experiments. Thank you for your patience and expertise.

My family has always believed in me and supported me through all the crazy things I've wanted to do. I am eternally grateful for the endless love and support my parents and brother have shown me throughout my life. This would not have been possible without them. I am so grateful for my village of family and friends who have provided me with friendship, support, and encouragement.

I would like to acknowledge Optical Society of America Biomedical Optics Express for permission to use portions of work published in their journal in Chapter 2-4 of this dissertation. I would also like to acknowledge the funding sources that contributed to this work, which include the NIH- R00EB007241 , NIH-K08NS059674, NIH-R01NS081243, seed funding from the UCR Office of Research and Development, UCR graduate research mentoring fellowship, and NSF IGERT: DGE 0903667. I would also like to thank the International Society for Optics and Photonics (SPIE) for the officer travel grant and UCR's Earle C. Anthony travel grant to attend SPIE Photonics West conferences.

ABSTRACT OF THE DISSERTATION

The Development of Optical Coherence Tomography to Study Optical Changes of Cortical Tissue During Seizures

by

Melissa Marion Eberle

Doctor of Philosophy, Graduate Program in Bioengineering
University of California, Riverside, August 2015
Dr. B. Hyle Park, Chairperson

High-resolution, minimally invasive imaging techniques are vital in visualizing and understanding the functionality of the brain. Scattering is the dominant source of light attenuation in biological tissue, making a reflective imaging technique ideal for studying changes in the optical properties of cortical tissue. Optical coherence tomography (OCT) is a high-resolution, minimally-invasive, imaging technique, capable of producing depth-resolved, cross-sectional, 2D and 3D images and has shown to be a promising method for *in vivo* imaging in highly scattering tissues such as the cerebral cortex. The goal of the research presented here was to develop OCT as a tool to study the optical changes of cortical tissue during induces seizures *in vivo* and *in vitro*. Initially, the average intensity changes were observed from 2D images during the induction of global seizures *in vivo*. A significant decrease ($P < 0.001$) in intensity during seizures was observed before the onset of generalized seizures. Next, the spatiotemporal resolution of OCT was fully utilize to visualize changes in the cerebral cortex optical properties through the development of 3D functional OCT (*f*OCT) images of intensity changes. A focal seizure

model was also introduced, and significant decreases in intensity were observed in both models. To further characterize the optical changes observed in cortical tissue, depth-resolved attenuation coefficient volumes were calculated. A confidence interval statistical analysis method was developed creating *f*OCT volumes to localize and quantify regions with significant changes in attenuation coefficient values during the progression of both seizure models. From the *f*OCT volumes, depth-dependent increases and decreases in attenuation coefficients were localized. To compare the electrical and optical temporal evolution, implanted electrodes were included for EEG analysis. Lastly, to investigate the biological mechanisms eliciting the changes in attenuation observed during seizure, phase-resolved Doppler OCT was used to show that attenuation values in tissue increase to match values within blood vessels. Second, *in vitro* seizure experiments were conducted showing the presence of changes in attenuation independent of blood. The results from this work demonstrate the potential utility of OCT as a minimally-invasive tool for studying seizure onset and propagation with high spatiotemporal resolution.

TABLE OF CONTENTS

LIST OF FIGURES

Chapter 1. Introduction and Background of OCT

1.1. Optical Coherence Tomography (OCT)

The development of optical imaging techniques that can provide noninvasive imaging of biological tissue with micrometer to millimeter imaging depths and micrometer resolution has helped advance a wide range of research and medical fields [1,2]. Optical coherence tomography (OCT) is one such technique that was first developed in the 1990's and used to investigate the thickness of retinal layers *in vivo* [3–11]. OCT uses low-coherence interferometry to create high-resolution, cross-sectional images of the intrinsic reflectance from biological tissue. Figure 1.1 illustrates how OCT compares in resolution versus imaging depth to other common imaging techniques used in the medical and research fields. Clinical imaging techniques such as functional magnetic imaging (fMRI), computed tomography (CT), and positron emission tomography (PET), have large imaging depths (tens of centimeters) and can image entire organisms, but have limited spatial resolution (millimeters) [1,2,12–18]. Ultrasound and especially high-frequency ultrasound have improved resolution (100 micrometers) while still maintaining large imaging depths of a couple centimeters [19]. When moving into the optical imaging regime, the resolution improves to single micron and submicron resolution, but the imaging depth is restricted to the upper few hundred microns. OCT bridges the gap between these commonly used imaging techniques by achieving micrometer resolution while maintaining an imaging depth of a few millimeters.

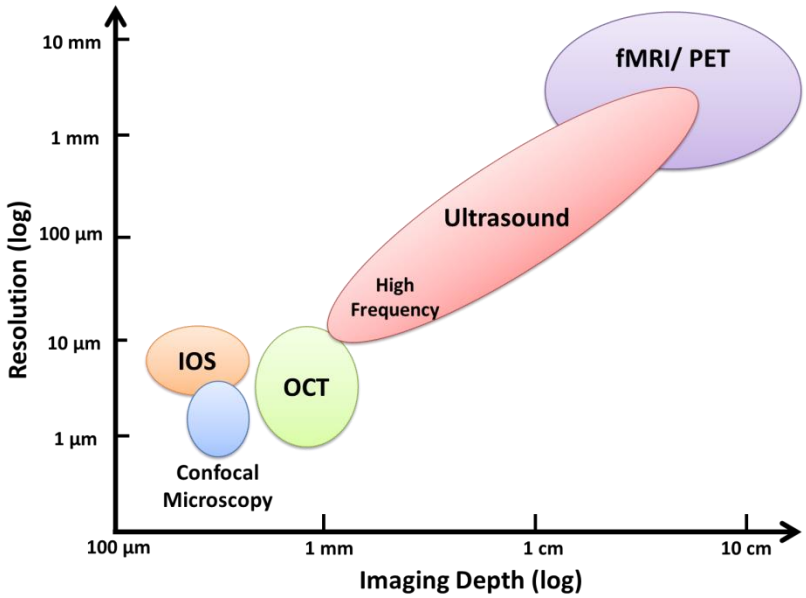

Figure 1.1: Comparison of resolution and imaging depth for functional magnetic resonance imaging (fMRI), positron emission tomography (PET), ultrasound, OCT, intrinsic optical signal imaging (IOS), and confocal microscopy.

1.2. Principles of OCT

OCT is an optical analog of ultrasound imaging, in which the magnitude and delay of backscattered waves reflected from within a sample are used to generate depth-resolved reflectivity images. The fact that light travels much faster than sound makes direct differentiation of light "echoes" from different depths within a sample impossible. This necessitates the use of low-coherence interferometry to detect the intensity and optical path delay in OCT [20]. Interferometry creates interference patterns between light that is backscattered from a sample and light reflected from a known reference path length.

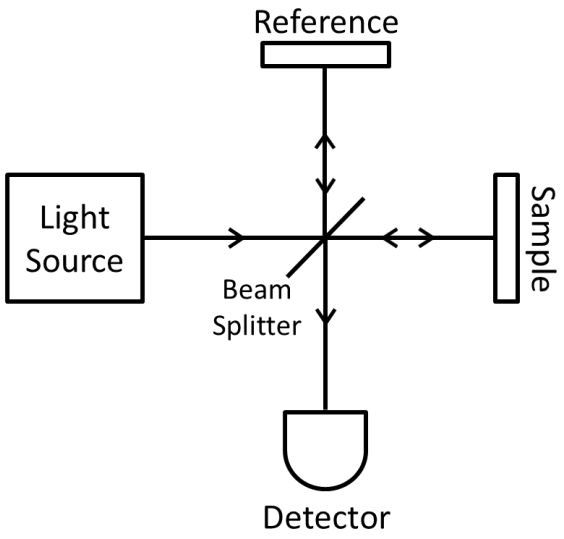

Figure 1.2: Schematic of a Michelson Interferometer with a beam splitter.

In a Michelson interferometer, light is split between a reference path $E_R(t)$ and a sample path $E_s(t)$ before being reflected, interfered, and sent to a detector arm (Figure 1.2). The intensity (I_d) at the detector is proportional to the sum of the square of the total field [21]:

$$I_d \sim |E_R|^2 + |E_s|^2 + 2E_R E_s \cos(2k\Delta L) \tag{1.1}$$

The interference term is dependent on the path length difference (ΔL) between the sample and reference arms. In OCT, gating in the axial direction is achieved by the use of a low-coherence, broad-bandwidth light source. The path length differences must be within the coherence length of the light source ensuring interference over only the coherence length.

In time-domain OCT (TD-OCT), the reference arm is scanned to obtain a depth profile (A-line) from the sample, which is generated by demodulation of the resulting time-resolved interferogram. Through scanning the incident beam across the sample and collecting sequential depth profiles, 2D cross-sectional imaging can be performed. 3D

imaging can be performed by raster scanning the beam across the sample taking consecutive 2D images (Figure 1.3).

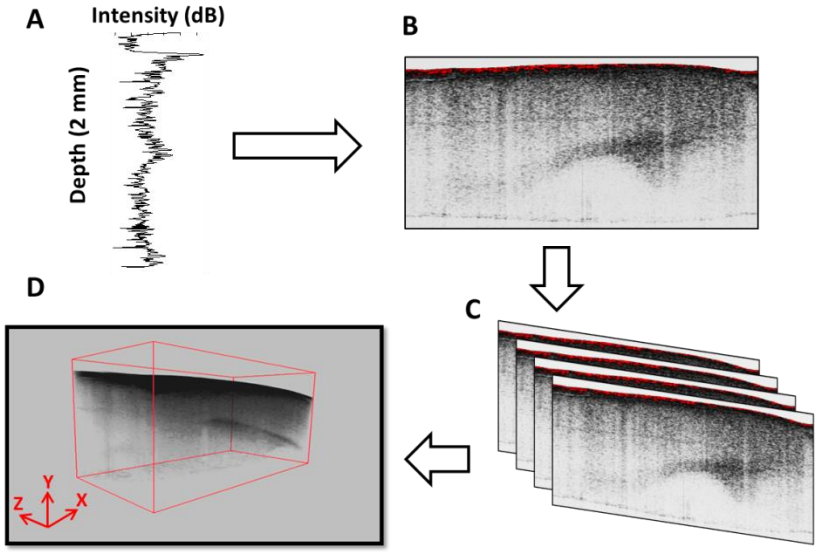

Figure 1.3 OCT image and volume construction. (A) A-line plotted in depth vs. dB (B) cross-sectional images composed of 2048 A-lines of cortical tissue with the intensities on a logarithmic inverse gray scale (C) stacks of sequential images (D) a 3D volume rendering of 200 consecutive cross-sectional images.

TD-OCT was the first generation of OCT systems [5,8,10,11,22], however, due to limited sensitivity and physical limitations of the mirror scanning speed, depth profile acquisition with this methodology is limited to several thousand hertz [23], making video rate image acquisition difficult. The major advancement of OCT was in the development of Fourier Domain OCT systems such as spectral-domain (SDOCT) and swept-source (SSOCT) (also called optical frequency domain imaging or OFDI) [3,4,6,7,9,23–25].

1.3. Spectral Domain- Optical Coherence Tomography

Spectral Domain-OCT (SD-OCT) uses a broadband, continuous wave source and the reference and sample arms are fixed to nearly the same optical path length. The interference pattern is detected in a spectrally-resolved manner. Fourier transformation of the interferogram yields a depth-resolved intensity profile. This has a number of

significant advantages over TD-OCT detection: an order of magnitude improvement in detection sensitivity that can be used to increase acquisition speed, simultaneous acquisition of information at all depths, and improved system stability resulting from a stationary reference arm configuration [3,6,9].

A fiber optic SD-OCT system is illustrated in Figure 1.4 [26] with a light source composed of two superluminescent diodes (SLDs) centered at 1298 nm, the longer wavelength allowing for deeper imaging depth due to a longer mean free path between scattering events and a local minimum in the water absorption spectrum. This provides an imaging depth up to two millimeters in highly scattering tissue [27]. From the source, the light is sent through a circulator (cr) and then split with an 80/20 fiber coupler between the sample and reference arm. The reflected light from both arms is then recombined and the now interfered light is sent back through the circulator to the spectrometer where it is collimated, dispersed by a grating, and the spectral lines are focused on a 1024 pixel line scan camera (lsc). Scanning of the optical beam to perform 2D and 3D imaging is done through galvanometer mounted mirrors (gm) in the sample arm.

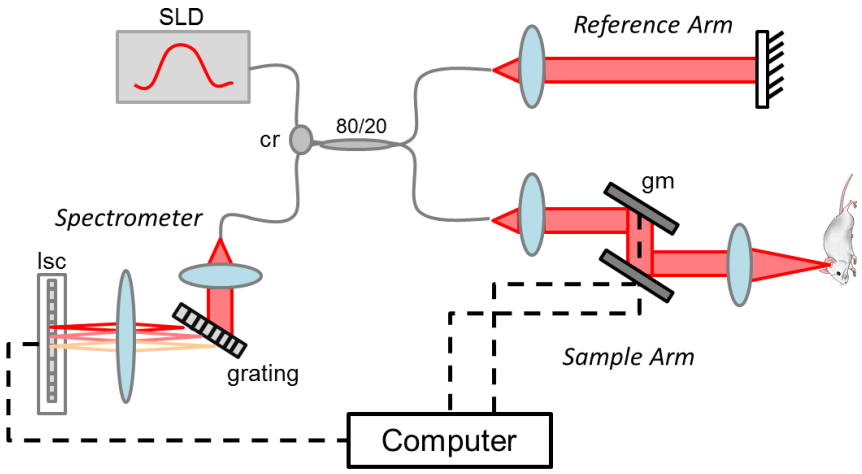

Figure 1.4: Schematic of the SD-OCT system. SLD: superluminescent diodes, cr: circulator, lsc: line scan camera, gm:galvanometer.

As described in Section 1.2, the intensity at the detector I_d is the square of the sum of the of the returning reflection electric fields from both the sample arm E_s and the reference arm E_R, which can be expressed as:

$$I_d(k,\omega) = \frac{\rho}{2}\langle|E_R + E_s|^2\rangle \tag{1.2}$$

where ρ represents the detector sensitivity, the factor of 2 accounts for the second pass of each field through the beamsplitter, and the angular brackets denote the integration over the response time of the detector. Assuming a polychromatic plane wave source, the incident electric field can be expressed as $E_i = s(k,\omega)e^{i(kz-\omega t)}$, where $s(k,\omega)$ is the electric field amplitude as a function of the wavenumber $k = 2\pi/\lambda$ and angular frequency $\omega = 2\pi\nu$. Reflections along the sample beam axis $r_s(z_s)$, where z_s is the pathlength of the reflection measured from the beamsplitter, are generally continuous in biological tissue and can be complex encoding the phase as well as the amplitude of the reflections. For simplification, we assume a series (N) of real delta-function reflections of the form: $r_s(z_s) = \sum_{n=1}^{N} r_{Sn}\,\delta(z_S - z_{Sn})$, with each reflection characterized by its electric

field reflectivity r_{Sn} and the pathlength (z_s) from the beam splitter, where $z = 0$. Using this simplification and expanding for the detector current, the reflections of the electric fields from the sample and reference arm are expressed in terms of the incident field as:

$$E_R = \frac{s(k,\omega)}{\sqrt{s}} r_R e^{i(2kz_{r-}\omega t)} \tag{1.3}$$

$$E_s = \frac{s(k,\omega)}{\sqrt{s}} \sum_{n=1}^{N} r_{Sn} e^{i(2kz_{Sn-}\omega t)} \tag{1.4}$$

If Equations 1.3 and 1.4 are substituted back into Equation 1.2 then expanding the squared functions give the following equation for I_D:

$$\begin{aligned} I_D(k) &= \frac{\rho}{4}[S(k)(R_R + R_{Sn} + \cdots)] \\ &+ \frac{\rho}{4}\left[S(k)\sum_{n=1}^{N}\sqrt{R_R R_{Sn}}\left(e^{i2k(z_R - z_{Sn})} + e^{-i2k(z_R - z_{Sn})}\right)\right] \\ &+ \frac{\rho}{4}\left[S(k)\sum_{n\neq m=1}^{N}\sqrt{R_{Sn} R_{Sm}}\left(e^{i2k(z_{Sn} - z_{Sm})} + e^{-i2k(z_{Sn} - z_{Sm})}\right)\right] \end{aligned} \tag{1.5}$$

A Gaussian function $S(k) = \langle |s(k,\omega)|^2 \rangle$ is used to model the source spectrum and then using Euler's rule to simplify Equation 1.5 generates a real result for I_D as a function of wavenumber creating a "spectral interferogram" expressed as:

$$\begin{aligned} I_D(k) &= \frac{\rho}{4}[S(k)(R_R + R_{Sn} + \cdots)] \\ &+ \frac{\rho}{4}\left[S(k)\sum_{n=1}^{N}\sqrt{R_R R_{Sn}}(\cos[2k(z_R - z_{Sn})])\right] \\ &+ \frac{\rho}{4}\left[S(k)\sum_{n\neq m=1}^{N}\sqrt{R_{Sn} R_{Sm}}(\cos[2k(z_{Sn} - z_{Sm})])\right] \end{aligned} \tag{1.6}$$

The first term in Equation 1.6 is the power reflectivity from the reference mirror plus the sum of the sample reflectivities and is referred to as the DC component. The second term is the cross-correlation or interferometric term of the path length difference between the

reference arm and each sample reflector with respect to the source wavenumber. The frequency of the cosine encodes the axial location of the scatterer. The third term is the auto-correlation term between the different reflectors within the sample. In the case of multiple reflectors in the sample, the spectrum is modulated by multiple cosineusoids with a frequency and amplitude corresponding to each sample reflection.

In SD-OCT all the spectral components of $I_D(k)$ are captured simultaneously on the line scan camera at the output of the spectrometer arm. Depth resolved reflectivity is constructed through the inverse Fourier transform of $I_D(k)$ utilizing the Fourier transform pair $\frac{1}{2}[\delta(z+z_o)+\delta(z-z_o)] \overset{F}{\leftrightarrow} \cos kz_o$ and the convolution property of Fourier transforms $x(z) \otimes y(z) \overset{F}{\leftrightarrow} X(k)Y(k)$. The inverse Fourier transform of Equation 1.6 is calculated as:

$$\begin{aligned} i_D(z) &= \frac{\rho}{8}[\gamma(z)(R_R + R_{Sn} + \cdots)] \\ &+ \frac{\rho}{4}\left[\gamma(z) \otimes \sum_{n=1}^{N} \sqrt{R_R R_{Sn}}(\delta[z \pm 2(z_R - z_{Sn})])\right] \\ &+ \frac{\rho}{8}\left[\gamma(z) \otimes \sum_{n \neq m=1}^{N} \sqrt{R_{Sn} R_{Sm}}(\delta[z \pm 2(z_{Sn} - z_{Sm})])\right] \end{aligned} \tag{1.7}$$

where the coherent function $\gamma(z)$ is the FT^{-1} of the Gaussian source function *S(k)* defined as:

$$\gamma(z) = e^{-z^2\Delta k^2} \overset{F}{\leftrightarrow} S(k) = \frac{1}{\Delta k\sqrt{\pi}} e^{-\left[\frac{(k-k_O)}{\Delta k}\right]^2} \tag{1.8}$$

where k_o represents the central wavenumber of the light source spectrum and Δk is the spectral bandwidth. Carrying out the convolution of Equation 1.7 we obtain the final depth resolved reflectivity profile referred to as an "A-line":

$$i_D(z) = \frac{\rho}{8}[\gamma(z)(R_R + R_{Sn} + \cdots)]$$

$$+\frac{\rho}{4}\left[\sum_{n=1}^{N}\sqrt{R_R R_{Sn}}(\gamma[2(z_R - z_{Sn})] + \gamma[-2(z_R - z_{Sn})])\right] \quad (1.9)$$

$$+\frac{\rho}{8}\left[\sum_{n\neq m=1}^{N}\sqrt{R_{Sn}R_{Sm}}(\gamma[2(z_{Sn} - z_{Sm})] + \gamma[-2(z_{Sn} - z_{Sm})])\right]$$

With the assumption of a Gaussian source, the axial point-spread function (PSF) is characterized by its full width at half the maximum (FWHM) value and defines the round trip coherence length of the light source l_c and is defined as:

$$l_c = \frac{2\sqrt{\ln(2)}}{\Delta k} = \frac{2\ln(2)}{\pi}\frac{\lambda_o^2}{\Delta\lambda} \quad (1.10)$$

for both wavenumber and wavelength, where λ_o is the center wavelength of the source and $\Delta\lambda$ is the bandwidth and has an inverse relationship to the coherence length, which defines the axial resolution of the OCT system. The optics used in the sample arm dictate the lateral resolution of the system.

1.3.1. Autocalibration for accurate wavelength assignment

The spectrometer does not evenly distribute the spectral interferogram, described by Equation 1.9, across the lsc, which is necessary in order to perform the FT^{-1} from wavenumber (k) to distance (z) [28]. Proper wavelength assignment can be achieved by introducing a perfect sinusoidal modulation as a function of k by passing light through a coverslip in the source arm. The wavelength mapping is determined by minimizing the nonlinearity of the phase of the perfect sinusoid through an iterative process [28]. The initial wavelength array W is used to interpolate the spectral interference fringes to equally spaced k values. The phase of the zero-padded, k- space interpolated spectrum is

determined and fitted with a third order polynomial. The nonlinear part $\sigma(k)$ of the polynomial fit is used for correcting the wavelengths W. Thus a new k-array, k', is calculated from the previous $k = 2\pi/W$ array and $\sigma(k)$:

$$k' = k + \sigma(k)/z_{peak} \tag{1.11}$$

where $z_{peak} = 2\pi PI/(k_{max} - k_{min})$. PI, or peak index, is the location of the coherence peak and k_{max} and k_{min} are the extremes of k. This correction, applied iteratively to the original spectrum, results in the wavelength array:

$$W' = 2\pi/k' \tag{1.12}$$

The wavelength array W' (Figure 1.5B) can be used to map the spectrum (Figure 1.5A) to the correct k values for each A-line (Figure 1.5C) [28]. After interpolation, the inverse Fourier transform is taken (Figure 1.5D).

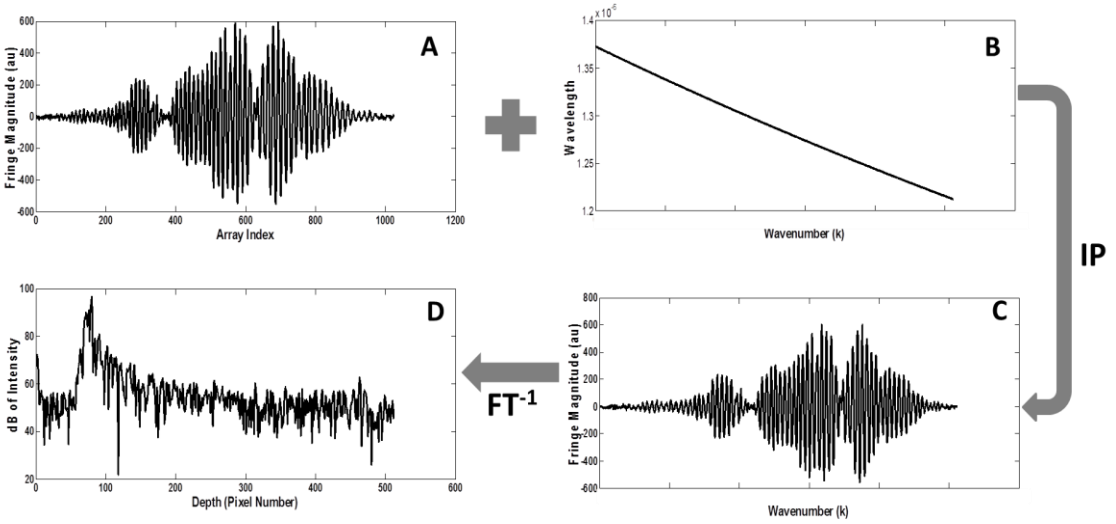

Figure 1.5: A-line preprocessing schematic. (A) Fringe magnitude with respect to the pixel array for one A-line. (B) Wavelength array W' with respect to wavenumber used to correct wavenumber assignment in each pixel in (A). IP: Interpolation step of A with respect to B. (C) Resulting fringe magnitude plot post IP with correct wavenumber assignment. FT^{-1}: inverse Fourier transform. (D) Resulting dB intensity A-line with depth (mirror image removed).

Also, in SD-OCT, the sensitivity of the system decreases as a function of depth due to the finite resolution of the spectrometer. Because of this, the sensitivity was measured and removed during image processing by multiplying each A-line by a calculated correction curve [7,9] to yield adjusted intensity images, a correction step necessary for accurate depth-dependent calculations.

1.4. Doppler OCT

Doppler OCT is a functional extension of OCT used to perform high-resolution mapping of fluid flow within biological tissue [29–32] . The velocity of the fluid flow can be determined from the phase information of the complex signal obtained after the Fourier transform of the interferogram through calculating the phase difference ($\Delta\varphi$) between two successive A-lines where *i* is the A-line number and *z* is depth position. The phase is corrected for the intensity-weighted mean phase difference and then the phase difference was calculated [33]:

$$\Delta\varphi_{i+1}(z) = \varphi_{i+1}(z) - \varphi_i(z) \tag{1.13}$$

$\Delta\varphi_{i+1}$ was phase-unwrapped and the bulk motion of individual phase values are corrected for

$$\varphi_{i+1,new}(z) = \varphi_{i+1}(z) - \left(\sum_z I_{i+1}(z)\Delta\varphi_{i+1}(z)/\left(\sum_z I_{i+1}(z)\right)\right) \tag{1.14}$$

The new phase values for each A-line were again corrected for phase wrapping ($\Delta\varphi_i'$). Lastly, the bi-directional phase is calculated through an intensity-weighted normalization:

$$\omega_i(z_i) = \frac{|I_i(z_i)|^2\Delta\varphi_i'(z_i)}{|I_i(z_i)|^2} \tag{1.15}$$

The values of the phase difference range from $-\pi$ to π and dictate the direction of flow. Phase variance images are generated through squaring the generated phase difference:

$$Var_i(z_i) = \frac{|I_i(z_i)|^2 \Delta\varphi_i'(z_i)^2}{|I_i(z_i)|^2} \tag{1.16}$$

The values of the phase difference range from 0 to π^2 and are only an absolute presence of flow and are used for the reconstruction of high-resolution images of flow.

1.5. Neuroimaging and OCT applications

High resolution and minimally-invasive imaging techniques have been vital in understanding and visualizing the functionality of the brain *in vivo* [1,2,34].Clinical imaging techniques such as functional magnetic imaging (fMRI), positron emission tomography (PET), computed tomography (CT), and ultrasound are widely used in investigating the structure and function of the brain, but have limitations with regards to image resolution, acquisition speed, and specificity [1,2,12–19].

Examples of functional imaging techniques developed in order to capture cortical dynamics *in vivo* are Positron Emission Tomography (PET) and genetically encoded calcium indicators (GECIs) [12,17,35,36]. PET can acquire millimeter resolution with functionally labeled substrates but lacks structural image information if not paired with another imaging modality such as MRI or CT [12]. Furthermore, the labeling agents are positron-emitting radionuclides that can have toxic side effects. GECIs can achieve single cell resolution with fluorescent, confocal, or two-photon imaging and can functionally control the activation and deactivation of select groups of cells. However, degradation

due to optical scattering limits the imaging depth to a few hundred micrometers and genetically engineered proteins are required altering the native biology [35,36].

Optical imaging techniques such as intrinsic optical signal (IOS) [37–42], diffuse optical imaging and tomography [43–46], photoacoustic tomography and microscopy [47–50], and spatial frequency domain imaging (SFDI) [51] overcome these limitations by achieving high-resolution, minimally invasive, imaging of the occurrence and propagation of neuronal and epileptic activity through changes in intrinsic tissue optical properties.

Optical coherence tomography (OCT) is a label-free, high-resolution, minimally-invasive imaging technique, which can produce depth-resolved, cross-sectional 2D and 3D image data [3–9], bridging the gap between clinical and microscopy imaging techniques (Figure 1.1). These combined traits make OCT an ideal imaging technique for functional localization of the intrinsic optical change of cortical tissue associated with neural activity and has been shown to be a promising method for *in vivo* imaging in highly scattering tissues such as the cerebral cortex [22,27,34,48,52–61].

Chapter 2. *In vivo* detection of cortical optical changes associated with seizure activity with optical coherence tomography

2.1. Introduction

Epilepsy, affecting at least 2% of the population [62], encompasses a group of disorders of the brain characterized by the periodic and unpredictable occurrence of seizures. As seizures are intermittent in patients with epilepsy, detection of seizures before they occur would be revolutionary in both warning patients and also developing "closed-loop" seizure detection and termination paradigms. To date, seizure detection algorithms have been solely based on analysis of either surface or intracranial electroencephalography (EEG). However, EEG has low spatial resolution, minimal depth discrimination and high susceptibility to electrical noise and motion artifacts. While great efforts are underway, there are currently no real-time methods of EEG analysis capable of reliably and reproducibly predicting seizure onset [63,64].

Optical techniques using near-infrared (NIR) light have been implemented to improve upon EEG technology by decreasing noise and increasing spatial and temporal resolution [51,65]. Previous research has suggested that optical changes, specifically changes in near-infrared optical scattering, may precede EEG seizure onset in animal models and that these optical changes are due to pre-seizure physiological changes, in particular reduction in the extracellular space [51,66,67]. Due to changes in the optical properties of the tissue, a decrease in intensity of backscattered light has been observed during the progression of seizures using noncontact NIR imaging and fiberoptic probes [51,68].

Optical coherence tomography (OCT) is a high resolution, minimally invasive, imaging technique which uses the short temporal coherence of a broadband light source to create cross-sectional images in real time [5,8]. OCT has shown to be a promising method for *in vivo* imaging in highly scattering tissues such as the cerebral cortex and several groups have demonstrated that through functional OCT imaging, changes in tissue composition can be detected optically during stimulation [52,58–60,69]. In this study, we demonstrated that changes in the optical properties of brain tissue during the progression of seizures can be detected with the use of spectral-domain optical coherence tomography (SD-OCT) [4] by inducing a generalized seizure, measuring the changes in the intensity from the imaged tissue over time, and then quantifying these changes.

2.2. Materials and experimental methods

2.2.1. Animal preparation for in vivo experimentation

6-8 week old, CD1 female mice (25-35 g) were initially anesthetized intraperitoneally (i.p.) with a combination of ketamine and xylazine (80 mg/kg ketamine, 10 mg/kg xylazine) and anesthesia levels were carefully monitored via breathing rate and reflexes. A 4x4 mm thinned skull cortical window was created with a dental bur over the cerebral cortex [70]. The skull was thinned to a uniform 55 μm. The mice were then imaged and a 10 min baseline was collected before a saline control injection was administered. After 25 to 30 min, pentylenetetrazol (PTZ) (100 mg/kg) was injected i.p. to induce a seizure. PTZ is a $GABA_A$ antagonist that reproducibly causes generalized seizures in this mouse model with a latency after injection [71], allowing for the study of the optical characteristics of the post-injection, pre-seizure state. Once a generalized tonic-clonic

(stage-5) seizure was observed, involving fore- and hind-limb twitches and tail movement, the animal was sacrificed with an anesthesia overdose. All experimental procedures were approved by the University of California, Riverside Institutional Animal Care and Use Committee.

2.2.2. Spectral-domain optical coherence tomography (SD-OCT)

The SD-OCT system outlined in Chapter 1, [26] utilized a broadband source composed of two super-luminescent diodes (SLD), one centered at 1295nm with a full-width at half maximum (FWHM) bandwidth of 97 nm (Thorlabs Inc.) and the other centered at 1350 nm with a FWHM bandwidth of 48 nm (Denselight Semiconductors Pte Ltd). The combined source was centered at 1298 nm with a 120 nm FWHM bandwidth. The experimentally determined axial and lateral resolutions were 8 μm and 20 μm respectively. From the source, the light was sent to a fiber circulator (Thorlabs Inc.) and split with an 80/20 fiber coupler between the sample and reference arm. In the sample arm, a pair of galvanometer (gm) mirrors provided transverse scanning of a 10 μm diameter focused beam. The lens used to direct light to the sample (AC254-075-C, ThorLabs) had a 1 inch diameter with a focal length of 75 mm. The reflected light from both arms was then recombined at the coupler and the now interfered light was sent to a spectrometer with a transmission diffraction grating (1100 lines per mm, Wasatch Photonics) before being focused by a planoconvex lens onto a 1024 pixel line scan camera (lsc, Goodrich SUI SU-LDH linear digital high speed InGaAs camera).

2.2.3. Image acquisition and data processing

To image the mouse brain, we continuously scanned the motor cortex region of the right hemisphere centered over the corpus callosum. An imaging depth of 2 mm was obtained with 6 mW of incident power and a focal point 1 mm below the thinned skull. Axial line scans (A-lines) were acquired at 15 kHz, with each cross-sectional image consisting of 2048 A-lines spanning a 3 mm imaging plane. The spectral data was then sent to the graphics processing unit (GPU) where, to correct for the nonlinear *k*-space sampling interval, 512 sampled points per A-line scan were mapped to uniform frequency spacing by linear interpolation [9]. The GPU also handled the Fourier-transformation into the spatial domain and secondary image processing, including plotting the intensity images on a logarithmic inverse gray scale (Figure 2.1) [26]. In SD-OCT, the sensitivity of the system decreases as a function of depth due to the finite resolution of the spectrometer and because of this, we applied a depth-correction function, reported by Yun *et al.* [9], during image processing by multiplying each A-line by a calculated correction curve. The resolution of the spectrometer is measured as a function of depth:

$$R(z) = \left(\frac{\sin\zeta}{\zeta}\right)^2 * e^{\left[-\frac{w^2}{2ln2}\zeta^2\right]} \tag{2.1}$$

where $\zeta = (\pi/2) * (z/z_{RD})$ is the depth normalized to the maximum ranging depth, $z_{RD} = \lambda^2/(4\Delta\lambda)$ where $\Delta\lambda$ is the wavelength spacing between pixels, and $w = \delta\lambda/\Delta\lambda$ where $\delta\lambda$ is the spectrometer's spectral resolution (FWHM). The resulting spectrometer dropoff was 11dB and the above equation was used to fit the dropoff and calculate the correction curve (See Appendix A1). By applying the depth-correction, it insured any

change in tissue intensity was caused by biological effects not axial movement of the sample in the imaging window.

2.3. Results and discussion

2.3.1. Calculating average intensities from regions of interest

To analyze the changes in backscattered intensity resulting from changes in tissue composition during seizure progression, we calculated average intensities from regions of interest (ROI) over time. Our images had a maximum SNR of 45 dB above the noise floor and when selecting our ROIs we were careful to avoid regions where the SNR dropped below 10 dB. The ROIs we selected were approximately 1 mm deep and 3 mm wide and included all the cortical tissue in the imaging window because we were interested in the overall trend in intensity exhibited by the tissue. Minor variations in the ROI shape do not affect the final average intensity due to the high intensities of the selected regions (Figure 2.1). To produce the results in Figure 2.1, an image was analyzed every 10 s and the average intensities, which were normalized to the 10 min baseline, were plotted versus time. We also used a reference reflector during our experiments and analyzed small ROIs over time to ensure any changes were from biological phenomena and not system artifact.

2.3.2. Experimental controls

When designing our experiment, we used two controls. The first was a time sequence of baseline measurements, which were obtained prior to any experimental injection over the course of 10 min. The second was a saline injection with a volume equivalent to the PTZ dosage. This injection directly followed the baseline and post injection data was acquired

for 25-30 min to establish if an injection alone causes a change in backscattered intensity from the imaged cortical tissue. In order to determine whether the saline injection caused any significant change in intensity, we calculated a two standard deviation (2SD) interval above and below the mean of the baseline spread and plotted the intervals in Figure 2.1 to establish a high and low threshold for the intensity data. Due to low variability in the baseline data for all four experiments, we are able to construct narrow threshold intervals allowing us to detect even minor changes in intensity throughout experimentation.

It is apparent that there is no significant change in intensity during our controls (Figure 2.1). To quantify our results, we calculated the baseline and post saline injection slopes through linear regression of the data in Figure 2.1B for all four experiments. The intervals, from which the baseline slopes were calculated, began at time zero and ended at saline injection and the post saline injection slopes were calculated from the administration of the saline injection to PTZ injection. The average baseline slope was -0.16×10^{-3} NI/t and the average post saline injection slope was -0.59×10^{-3} NI/t. We used a Tukey multiple comparisons test to compare baseline, post saline injection, and post PTZ injection slopes and our results indicated no significant change in intensity between baseline and post saline inj. with a *P*-value of 0.9997.

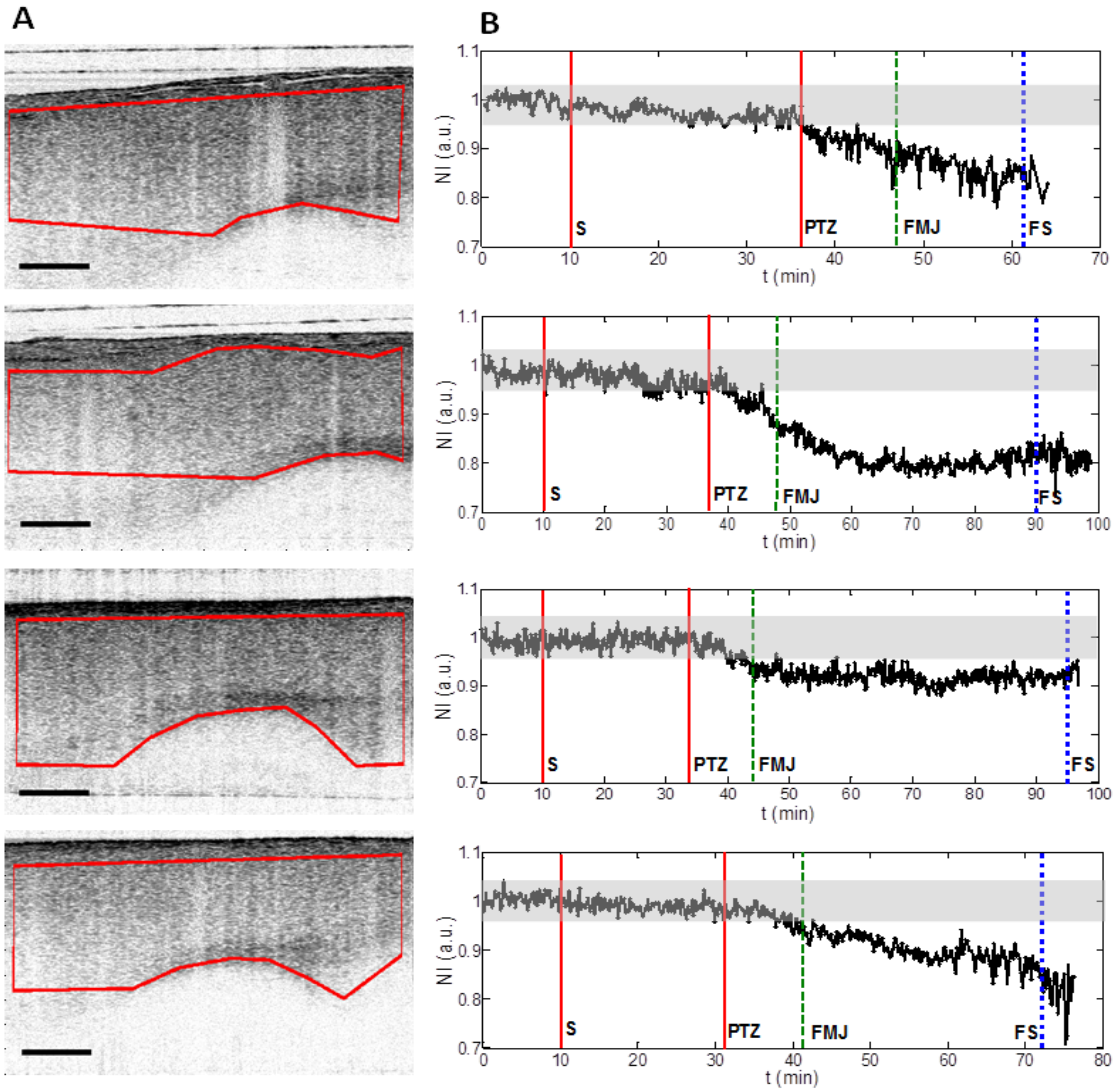

Figure 2.1: Reduction in intensity during seizure progression. (A) OCT images of mice brain, one for each experiment, acquired *in vivo*. The red boxes indicate the ROIs used for average intensity calculations. The scale bar is 0.5 mm. (B) Plots of normalized intensity (NI) from the ROIs on left over time. The occurrences of the experimental steps are indicated: S: Saline injection (first red bar), PTZ: PTZ injection (second red bar), FMJ: facial myoclonic jerks (green dashed line), FS: full stage-5 seizure (blue dashed line). The gray region is the 2SD interval above and below the mean of the 10 min baseline.

2.3.3. Detection of optical changes during seizure progression

Directly after the saline control, we administered the PTZ injection to induce a seizure. OCT images were continuously acquired through the onset of a stage-5 seizure. The same ROI analysis was performed as was done for the controls and the resulting average

intensities were plotted verses time in Figure 2.1B. In all four experiments, a decrease in backscattered intensity post PTZ injection was observed. This decrease from normal is due to the change in tissue composition, which precedes the onset of a seizure [66–68]. The average intensity in the ROI was monitored as it decreased below the 2SD threshold. Variability between when PTZ injection occurred and when the threshold was crossed in each experiment was due to the noise in the baseline spread from which the 2SD threshold was calculated (Figure 2.2). Soon after the threshold was crossed, we observed facial myoclonic jerks (FMJs) (Figure 2.1), which are events associated with the early stages of seizure progression [72]. The timing from when the threshold was crossed to when the FMJs were observed varied between experiments, ranging from 1 to 10 min. However, the threshold crossing always occurred at least a minute before the first observed FMJs**.** This indicated that a significant decrease in intensity from baseline can be detected with OCT before the onset of observable physical manifestations associated with early stages of seizures. Also, because of the narrow threshold interval, we detected a significant decrease in intensity, even in the experiments where the total percent decrease from baseline was under 10%.

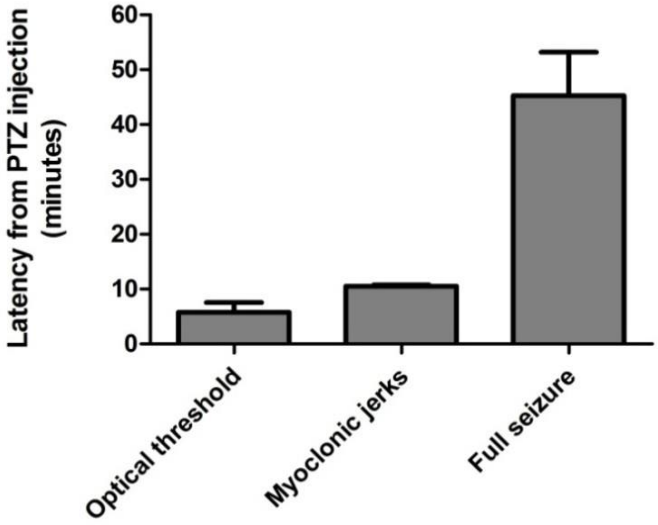

Figure 2.2: OCT-detected "optical threshold" precedes myoclonic jerks and full seizure. Latency from PTZ injection (min) displayed for optical threshold (defined as 2SD change in intensity), myoclonic jerks, and full stage-5 (generalized tonic-clonic) seizure. Optical threshold crossing preceded both myoclonic jerks (focal seizure) and generalized seizure, indicating the ability of OCT to optically detect pre-seizure state.

2.3.4. Analysis of changes during experimental steps

We imaged through the initiation of a stage-5 seizure, which due to the variability in anesthesia levels occurred at different time points after PTZ injection (Figure 2.2). As the seizures progressed, the intensity from the imaged areas continued to decrease. To quantify the changes in intensity, we calculated the slopes post PTZ injection for each of the four experiments using linear regression. The intervals for the slope calculations began at PTZ injection and ended once the data began to deviate from the linear decreasing trend. We then averaged the four slopes and plotted them in Figure 2.3 along with the baseline and post saline injection average slopes. The interval bars in Figure 2.3 were calculated by a 90% confidence interval (C.I.) using the t-distribution for small sample sizes. The average slopes and intervals for each of the three experimental steps

were: baseline -0.16 x 10^{-3} ± 0.99 x 10^{-3} NI/t, post saline inj. -0.59 x 10^{-3} ± 0.81 x 10^{-3} NI/t, and post PTZ inj. -5.3 x 10^{-3} ± 1.99 x 10^{-3} NI/t.

The differences in the slopes between experimental steps were analyzed with an ANOVA F-test and the results are summarized in Table 2-1. Even with slope variability between the four experiments, there is a significant difference between the treatments ($P < 0.001$), indicating that the mean slopes for all three steps are not equal.

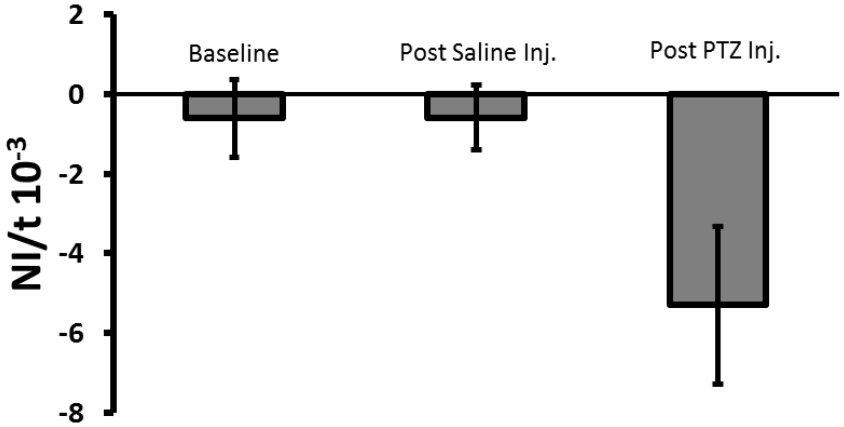

Figure 2.3: Plot of the three average slopes: Baseline, Post saline injection, and Post PTZ injection. The average slopes were calculated from four seizure experimental data sets. The interval bars were calculated with a 90% confidence interval using the t-distribution. NI: Normalized Intensity, t: time (min), Inj.: Injection

Table 2-1. ANOVA for the average slopes of the three experimental steps

	df	Sum of Square	Mean of Square	F-value	*P*-value
Treatment	2	5.98 x 10^{-5}	2.99 x 10^{-5}	22.34	1 x 10^{-4}
Error	9	1.2. x 10^{-5}	1.34 x 10^{-5}		

df: degrees of freedom

To explore the differences found with the ANOVA F-test, we performed a Tukey multiple comparisons test to compare the baseline, post saline, and post PTZ slopes (See Appendix A2). As mentioned previously in Section 2.3.2, the baseline and post saline

slopes were not significantly different. This procedure also compared the post PTZ injection slopes to the baseline and post saline injection slopes. The resulting *P*-values were $P < 0.001$ for both comparisons: post PTZ injection slope to the baseline slope and post PTZ injection slope to the post saline injection slope. This demonstrates that the change in backscattered intensity as a seizure progresses can be quantified and when compared with pre-seizure states, signifies that there is a significant decrease in intensity, detectable with OCT.

2.4. Conclusion

In conclusion, we conducted seizure experiments *in vivo* to establish, as a proof of principle, that a decrease in intensity during seizure progression can be detected through OCT imaging. We created a threshold interval model for the temporal identification of changes in the backscattered intensity. Our results indicated that crossing below the definable optical detection threshold occurred prior to either FMJs or generalized (tonic-clonic) manifestations of seizure activity. In the future, we plan on further developing this into an optical trigger to help identify the occurrence of seizures prospectively even before physical manifestations are present. These results could lead not only to optical seizure detection but also prediction with appropriate algorithmic real-time analysis of the OCT signal. Furthermore, previous research has used OCT to spatially resolve changes in cortical tissue during electrical stimulation [52,69] and by utilizing the high spatial and temporal resolution of OCT, it will be possible to map changes in intensity during seizure progression and propagation through the intact brain.

Chapter 3. 3D Visualization of Intensity Change Progression During Seizures in vivo

3.1. Introduction

There is a wide variety of imaging techniques used to image neuronal activity. Clinical imaging techniques such as fMRI, PET, CT and Ultrasound are widely used in investigating the structure and function of the brain, but have limitations with regards to image resolution, acquisition speed, and specificity [1,2,12–19]. Optical techniques such as OCT, IOS, DOT, SFDI, and confocal/fluorescent microscopy overcome some of these limitations by achieving high-resolution, targeted, video-rate imaging.

OCT is label-free, high-resolution, noncontact imaging technique, capable of producing depth-resolved, cross-sectional, three-dimensional (3D) volumes [3–9] and has been shown to be a promising method for *in vivo* imaging in highly scattering tissues such as the cerebral cortex [22,27,48,52–60]. In Chapter 2, we previously identified changes in the intensity of the cortex during the progression of induced generalized seizures *in vivo* in mice with OCT [53]. From each cross-sectional image, the average image intensity was calculated from a large region of interest, spanning 4 mm in the sagittal plane of the cerebral cortex and 1.5 mm in depth. By analyzing the temporal changes of these values, we observed significant decreases in the average intensity of cortical tissue preceding and during generalized tonic-clonic seizures induced with pentylenetetrazol (PTZ) [53].

The objective of this study was to expand on our previous findings by utilizing the spatiotemporal resolution of OCT in order to localize changes in the optical properties of murine cerebral cortex during seizure progression *in vivo* in both a global model (PTZ)

and a focal model (4-aminopyridine (4-AP)), which is known to induce localized seizures at the site of 4-AP injection. Sequential volumetric scans of the cortex were acquired for both global and focal animal models and the spatiotemporal progression of the percent change in intensity was determined highlighting the differences in seizure propagation between the two models. To compare the electrical and optical temporal evolution, we included implanted electrodes for EEG analysis in our 4-AP model.

3.2. Materials and experimental methods

3.2.1. Animal preparation for in vivo experimentation

Adult female (>6 weeks of age) CD1 mice were anesthetized with urethane (1.5 mg/g). The animals were then placed into a standard rodent stereotactic frame. Animals were kept on a heating blanket to maintain normal body temperature throughout the experiment. Anesthesia was maintained using a Ketamine/Xylazine mixture (80 mg/kg Ketamine, 10 mg/kg Xylazine) intraperitoneally (i.p.). Eight animals were used: two for the global model and six for the focal model (two control and four experimental). All experimental procedures were approved by the University of California, Riverside Institutional Animal Care and Use Committee.

3.2.1.1 Global seizure model

A 4 x 4 mm thinned skull cortical window was created with a dental bur over the cerebral cortex in the right hemisphere [70]. The skull was thinned to an approximately 55 μm throughout the window. OCT volumetric data was collected prior to i.p. injection of PTZ (100 mg/kg) and was collected through the entire experiment with an imaging window of 4 x 2 mm. PTZ is a $GABA_A$ antagonist that reproducibly causes generalized seizures in

this mouse model with a latency after injection [71]. Once a generalized tonic-clonic (stage-5) seizure was observed, involving fore- and hind-limb twitches and tail movement, the animal was sacrificed with an anesthesia overdose. Internal control measurements, prior to PTZ injection, were acquired with a 10 min baseline and 20 min post i.p. injection of saline (100 mg/kg). More extensive controls showed no significant change over 80 min in the same animal model with an $n = 3$ [73].

3.2.1.2 Focal seizure model

While the use of a thin skull cortical window better preserves the natural state of the brain, localized injections of 4-AP, a potassium channel blocker known to cause acute focal seizures at the injection site [38,41,74], required partial removal of the skull. After anesthesia induction, a linear midline skin incision was made on the scalp. A hemicraniectomy was performed to remove the bone between coronal suture and the lambdoidal suture. Animals then received intracerebral injections of 4-AP (15 mM) at a rate of 50 nl per minute for 10 minutes using a Nanoject II injector (Drummond Scientific) to induce focal seizures. The pipette was placed 0.5 mm into the cortical tissue and positioned 1.5 mm lateral and 1.0 mm caudal relative to bregma. The pipettes were custom pulled from 3.5" capillaries with a tip dimension of approximately 300 μm. Attached to the pipette and implanted into the tissue was a bipolar concentric electrode. Recording was continuously sampled at 5 kHz through the duration of the experiment with a MP 150 BIOPAC system and AcqKnowledge recording software.

OCT volumetric data was acquired through the entire experiments. The first two of the six animals were imaged with a 3 x 3 mm imaging window directly at the injection

site to ensure we observed any possible changes in intensity and attenuation during the focal seizure. Once we verified that we could in fact visualize these changes, we widened the imaging window to a 5 x 4 mm imaging window covering the hemicraniectomy region for the next four animals to visualize the spatial propagation of the changes from the site of injection. For the control experiment, artificial cerebrospinal fluid (ASCF) was substituted for the 4-AP injections.

3.2.2. Spectral- domain OCT

An SD-OCT system [3,4,6,9] optimal for imaging cortical tissue *in vivo*, utilizes a NIR light source centered at 1300 nm, providing an imaging depth of a few millimeters as well as achieving high spatial resolution [27]. The SD-OCT system used in this study is described in detail in Chapter 1 and Chapter 2 (see Figure 1.4) where the LED source was centered at 1298 nm with a 120 nm FWHM bandwidth. The experimentally determined axial and lateral resolutions were 8 μm and 20 μm respectively.

3.2.3. Image acquisition and OCT data processing

OCT volumetric data acquisition was performed with axial depth profiles (A-lines) acquired at 15 kHz. Two different acquisition protocols were used to either optimize the spatial or temporal resolution. To optimize the spatial resolution, a single volume of 200 sagittal cross-sectional images composed of 2048 A-lines was acquired every 2 minutes. To optimize the temporal resolution, a single volume of 150 images composed of 512 A-lines was acquired every 40 s. In either case, an imaging depth of 2 mm was obtained with 6 mW of incident power with a focal point 1 mm below the cortical surface. To correct for the nonlinear *k*-space sampling of the spectral data, 512 sampled points per A-

line scan were mapped to uniform wavenumber spacing by linear interpolation [28]. The fast Fourier-transformation (FFT) from wavenumber to spatial domain was performed as well as secondary image processing, including plotting the intensity images on a logarithmic inverse gray scale [26]. The depth-dependent sensitivity of SD-OCT acquisition was measured and then removed by multiplying each A-line by a calculated correction curve [7,9] to yield adjusted intensity images, a correction step necessary for accurate depth-dependent calculation described in Chapter 2. Our images had a maximum SNR of 35 dB and analysis was performed on regions with an SNR of at least 10 dB.

After initial OCT image processing, gross registration of sequential volumes was performed by maximizing the 3D cross-correlation with the initial volume of each data set. Registration was achieved through the following algorithm: Initially, the correlation matrices (r_C, r_F, r_G) were calculated. r_C was calculated through correlation of each preceding volume matrix G with the initial volume matrix F and r_F and r_G were calculated through correlation of each matrix F and G with themselves. This process was performed through the use of the Fourier transform ($\mathcal{F}$) method for matrix F and the complex conjugate matrix $\bar{G}$.

$$r_c = \mathcal{F}^{-1}[\mathcal{F}(F) * (\overline{\mathcal{F}(G)})] \tag{3.1}$$

Next, the matrix location of the maximum of the correlation matrix r_C was found, the volumes were shifted in all three dimensions with respect to the location of the maximum, and the correlation coefficient was calculated for each cross-correlation.

$$R = r_C / \sqrt{r_F * r_G} \tag{3.2}$$

Through the calculation and verification of correlation coefficients close to 1, we ensured accurate registration of the volumes throughout the experiment. A median filter of 64 x 64 μm was applied to minimize variations due to coherent speckle. This kernel size was determined starting from a cross-sectional area based on the lateral and axial resolutions, and iteratively expanded to determine the minimum cross-sectional area required to achieve a speckle contrast ratio (K_s) below 0.1 over a region of uniform cortical tissue.

$$K_s = \frac{\sigma_s}{\langle I \rangle} \tag{3.3}$$

K_s is defined as the ratio of the spatial standard deviation (σ_s) to the mean intensity. Thus, the lower σ_s is, the smaller the contrast ratio minimizing the effect of speckle.

3.3. Results and discussion

3.3.1. Global and focal control results

Control experiments were performed for both global and focal seizure models. To optimize the spatial resolution, a single volume of 200 sagittal cross-sectional images composed of 2048 A-lines was acquired every 2 minutes. We acquired 4 x 2 mm volumes and 3 x 3 mm volumes for the global and focal experiments respectively. After the collection of baseline volumes, the injection of either saline (global) or ACSF (focal) was administered. The timing of the injections is shown in Figure 3.1 along with the percent change in average intensity from selected 0.5 x 0.5 x 0.5 mm regions of interest (ROIs). Figure 3.1A shows two representative ROIs that were 1 mm lateral from each other and 1 mm from both the anterior and posterior of the volume. It should be noted that a total of 5 ROIs were analyzed in each set of data, with all exhibiting similar behavior. For the focal experiments (Figure 3.1B), ROIs were selected at the injection site and 1 mm lateral

and 2 mm posterior from the injection site. The mean of the baseline data in each model was used to calculate a two standard deviation (2SD) in the intensity change of ±2% for the global model (Figure 3.1A) and ±3% for the focal model (Figure 3.1B), plotted as red, horizontal, dashed lines in Figure 3.1, indicating the intrinsic fluctuation in the intensity values. The trend in the percent change in intensity stayed within the 2SD throughout the experiments for both the global and the focal models (Figure 3.1).

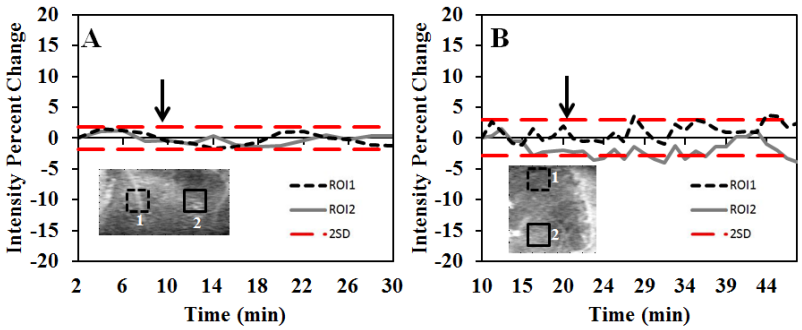

Figure 3.1 Percent change in average intensity for (A) Global and (B) Focal controls 0.5 x 0.5 x 0.5 mm ROIs. Global ROIs are separated 1 mm laterally outlined on the *en face* intensity image. Focal ROIs are located at the injection site (ROI 2) and 2 mm from the injection site (ROI 1) outlined on the *en face* intensity image. Arrows represent time of injection. Red horizontal bars: 2SD of the baseline mean. *En face* insets of a reference intensity volume. Top of image: Bregma, left of image: Rostral.

3.3.2. Change in intensity during global and focal seizures

Global and focal *in vivo* seizure experiments were conducted and in order to determine the changes in intensity during seizure progression from a pre-seizure state, an average baseline volume was calculated from five volumes (global) or three volumes (focal). The fractional intensity change of each following volume was computed by pointwise division of each volume by the average baseline volume. The square of the logarithm of the fractional changes were then computed in order to better visualize all changes in intensity from baseline, with the sign of the original logarithm reapplied after squaring. The ratio values in each pixel were scaled from black to color saturation at a

predetermined threshold value that represented a greater than ±50% change from baseline (blue represented ratios below baseline and red represented ratios above baseline) (Figure 3.2 and Figure 3.3). Three dimensional (3D) volumetric renderings of the spatiotemporal changes in intensity during both global (Figure 3.2) and focal (Figure 3.3) seizure progression were generated using Amira (FEI Visualization Sciences Group).

A representative result of the progression of changes in intensity can be seen in the rendered volumes following PTZ injection shown in Figure 3.2. Twenty-six minutes post injection, a significantly large decrease in intensity is apparent due to the accumulation of blue pixels throughout the imaged cortical tissue. The global nature of the decrease verifies the generalized nature of PTZ seizure progression. Representative results in Figure 3.3 from the focal seizure experiments show the progression of the intensity changes from the injection site, which is outlined in white at minute 12, following the last 4-AP injection. At 16 minutes post injections, a region of decreasing intensity initiates at the injection site. This significant decrease also corresponds with the onset of electrical seizure activity recorded at the site of injection from the implanted electrode, which is shown as the 1 min electrical trace below each frame in Figure 3.3. The blue pixels continue to accumulate indicating a significant decrease in intensity focused at the site of injection as the seizure continues to progress through the end of the experiment. The data for both the global and focal models were representative and the experiments were successfully repeated with similar results.

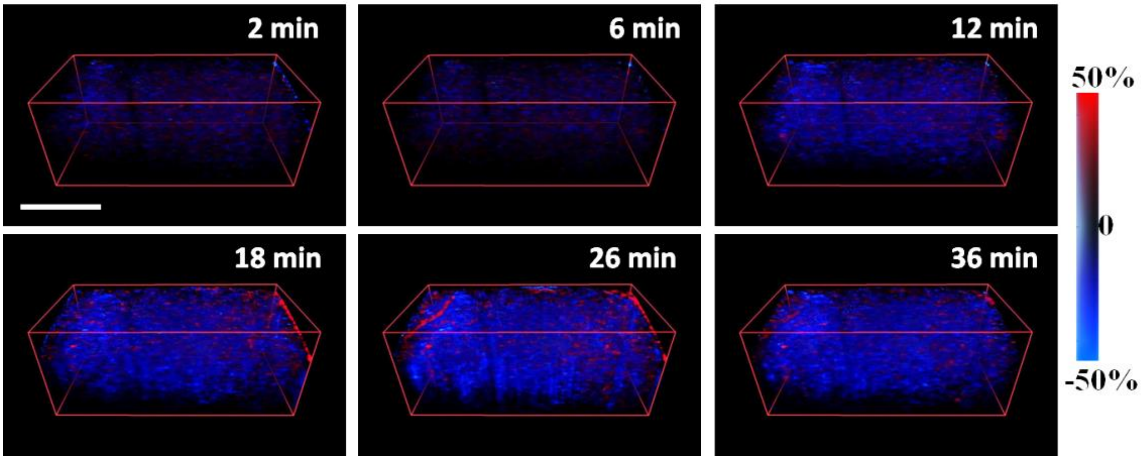

Figure 3.2 Volumes of change in intensity for the global seizure model. Volumes are 4 x 2 x 2 mm. Color bar: percent change from baseline (0%) saturating at ±50%. Time is min post-PTZ injection. Top of image: Bregma, left of image: Rostral. Scale bar: 1 mm.

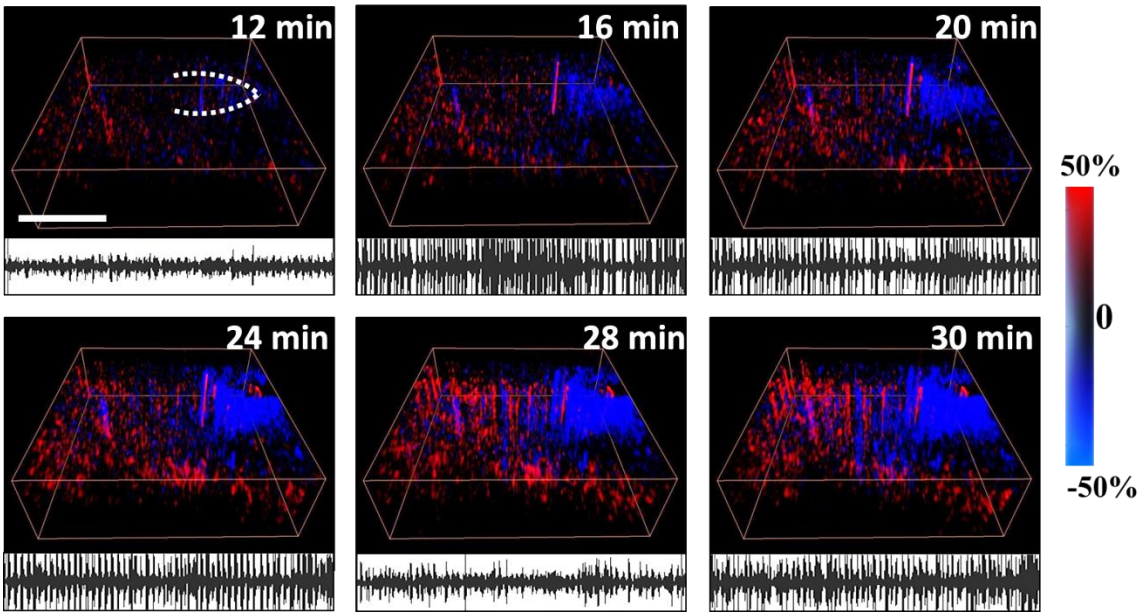

Figure 3.3 Volumes of change in intensity for the focal seizure model with their corresponding 1 min electrical trace ±1 mV displayed below. Volumes are 3 x 3 x 2 mm. Location of pipette injections is outlined in the first frame. Color bar: percent change from baseline (0%) saturating at ±50%. Time is min post 4-AP injections. Top of image: Bregma, left of image: Rostral. Scale bar: 1 mm.

In order to quantifiably differentiate the progression of the changes in intensity between the global and focal model, we analyzed the time course of the average fractional reflectivity from ROIs selected in the same manner as outlined in the control experiments (Figure 3.1). Figure 3.4A shows the location of the ROIs within the volume

for the global model and both ROIs show mirroring trends of decreasing intensity starting 6-8 min post-PTZ injection and reaching a maximum of 10-15% change from the baseline at full seizure onset 24 min post-PTZ injection. The animals were then given an anesthesia overdose at full seizure, which occurred at minute 29, and the average intensity began to return to baseline by the end of the experiment. In contrast for the focal model, a significant decrease in intensity occurred only in the ROI at the injection site starting 10 min post 4-AP injections, and reached a maximum 41% change 28 min post-injection. The two ROIs away from the injection site show no significant change in intensity outside the 2SD during the experiment. This analysis highlights the difference between the global and focal seizure spatiotemporal progression of changes in intensity during seizure progression.

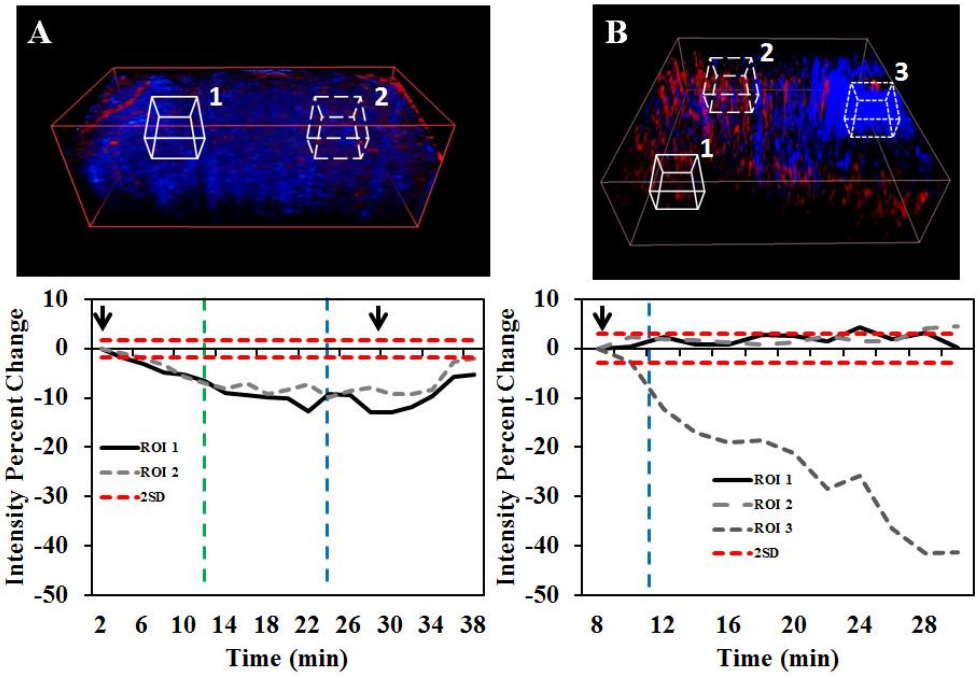

Figure 3.4 Global (A) and focal (B) seizure ROI analysis with the location of ROIs within the imaged volume and the intensity percent change plotted vs. time (A) post-PTZ and (B) post 4-AP injections along with each baseline 2SD as red, dashed, horizontal lines. (A) The first arrow is the time of PTZ injection the second is the anesthesia overdose. (B) Arrow is time of last 4-AP injection. The vertical dashed lines indicate stage-2 (green) and stage-5 (blue) seizures respectively. All ROIs are 0.5 x 0.5 x 0.5 mm.

3.4. Conclusion

In the global and focal seizure experiments, volumetric data was acquired and we demonstrated the ability of OCT to display the change in intensity in three dimensional volumes in time, preserving spatial specificity and accurately conveying the intensity trends occurring during seizure progression. In both seizure models, a large decrease in intensity occurred during seizure progression either throughout the cortical tissue (global model) or localized at the injection site (focal model). In the global model, the average percent decrease became statistically significant 6 min post PTZ injection and achieves a maximum percent decrease of 15% 24 min post PTZ injection. In the focal model, the average percent decrease became statistically significant 10 min post 4-AP injection and

reached a maximum 41% change at minute 28. These results, combined with the electrical recording for verification of seizure, coincide well with reflectance changes found in previous work with OCT as well as other imaging techniques and are a result of interconnected biological changes in absorption and scattering associated with hemodynamic responses and neuronal and glial swelling [38,39,43,44,51–54,58,59].

Chapter 4. Localization of Depth-Resolved Changes in Attenuation Coefficient for Visualization of Seizure Propagation *in vivo*

4.1. Introduction

Light is attenuated when propagating through tissue due to scattering and absorbing components of the tissue composition. The amount of attenuation that occurs is characterized by the attenuation coefficient (μ), which can be calculated from Lambert-Beer's law:

$$L(z) = L_0 e^{-\mu z} \tag{4.1}$$

where *L(z)* is the irradiance of the beam after traveling through the tissue over a distance *z* and L_0 is the incident irradiance. Because the attenuation coefficient is an optical property of the tissue, calculating it provides valuable characterization of the tissue composition [75]. Previous methods for determining the attenuation coefficient from OCT image data was to fit the exponential decay of A-lines acquired during imaging. Extensive lateral averaging or sampling is essential for a reliable fit requiring extensive segmentation of the data to ensure averaging over a uniform region of tissue. This method results in the reduction of a 2D image into a single attenuation coefficient value, losing the spatial and depth-resolved imaging that OCT provides.

In this study, we utilized a recently published method for determining per-pixel depth-resolved tissue attenuation coefficient images [75] for further understanding of the optical change through improved characterization of cortical tissue during the progression of the global and focal experiments described in Chapter 3 [76]. We then applied a confidence interval statistical analysis method to further quantify and localize regions

within the attenuation volumes with significant changes during the progression of both seizure models. Through the development of functional OCT (*f*OCT) volumes, we were able to visualize and further localize the spatiotemporal propagation of changes in attenuation coefficient in the cortical tissue.

4.2. Materials and experimental methods

4.2.1. Animal preparation for in vivo experimentation

For animal preparation and protocol see Chapter 3.2.1.

4.2.2. Image acquisition and OCT data processing

For image acquisition and processing protocol see Chapter 3.

4.2.3. Depth-resolved attenuation coefficient volumes

We calculated depth-resolved, per-pixel attenuation coefficient values ($\mu[i]$) (**Error! Reference source not found.**) for each volume using the algorithm described by Vermeer *et al.* [75]. The attenuation coefficient for a certain pixel was defined as:

$$\mu[i] = \frac{1}{2\Delta}\log\left(1 + \frac{I[i]}{\sum_{i+1}^{\infty} I[i]}\right) \tag{4.2}$$

where Δ is the pixel size and the attenuation coefficient in a pixel is defined by the average attenuation over the pixel size. For image processing, we subtracted the noise floor signal and then applied the depth-correction curve. We also assumed a tissue refractive index of 1.4. The attenuation coefficients found for gray and white matter ranged between 1-4 mm^{-1} and 4-8 mm^{-1}, respectively, and are comparable to previously published data [55,73] (See Appendix A3). Figure 4.1 highlights how difficult it would be to fit the different regions of the cortical tissue from the average intensity A-lines and

that through the depth-resolved attenuation coefficient processing discrete values are assigned for tissue with differing attenuating characteristics.

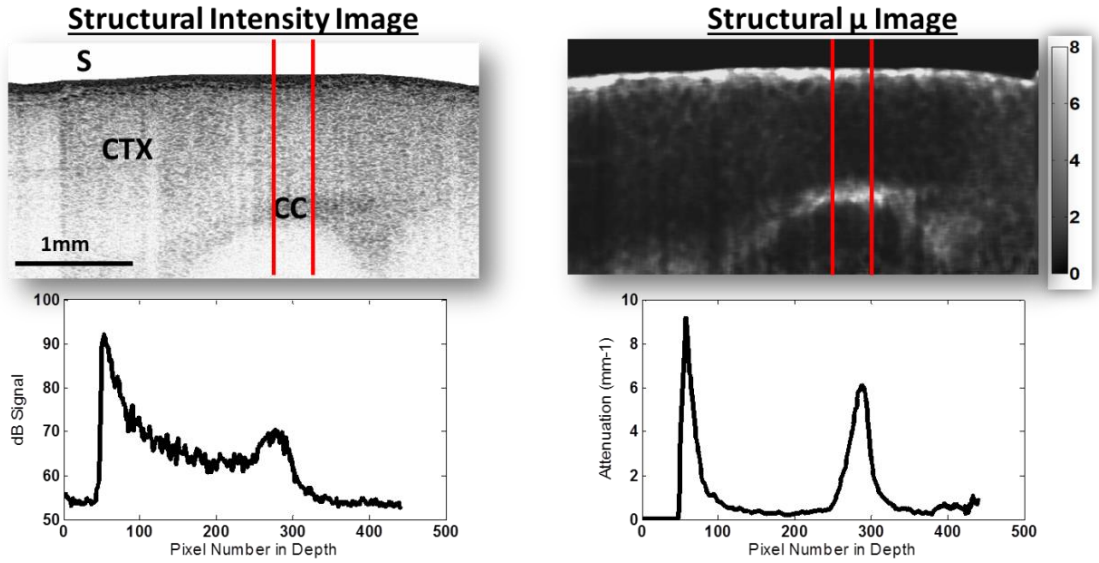

Figure 4.1Intensity (left) and the corresponding attenuation coefficient (right) sagittal image of mouse brain tissue. Color bar: μ in mm^{-1}. Below: average of 200 A-lines of intensity and attenuation within the region indicated by the red lines (identical regions for both intensity and attenuation). S: skull, CTX: cerebral cortex and CC: corpus callosum.

4.2.4. Statistical analysis for fOCT volume visualization

A confidence interval (C.I.) analysis was used in order to highlight only the attenuation values that represent a statistically significant deviation outside the range of natural and speckle induced variations in attenuation. Baseline volumetric data acquired prior to seizure initiation was used to generate the confidence intervals with the mean ($\bar{x}$) and standard error (SE) calculated from 30 x 30 x 30 μm voxels. The SEs were calculated from the sample standard deviation in each voxel (s) and the number of baseline volumes (n). The confidence level (0.90 or 0.95) chosen for each experiment's C.I. analysis was based on the baseline degrees of freedom (df), defined as ($n-1$), dictating which t^* value was selected to ensure a similar t-distribution for all experiments (See Appendix A4).

$$C.I. = \bar{x} \pm t^{*}SE, SE = s/\sqrt{n} \quad (4.3)$$

Once the boundaries of the C.I.s were determined, the mean in each voxel ($\bar{x}$) for each post-baseline volume was compared to the C.I. defined for the voxel. If the mean value fell above or below the C.I., then the percent change from maximum or minimum, respectively, of the C.I. was calculated as:

$$\Delta\mu = 100 \times \left(\bar{x}(x,y,z,t) - CI_{max,min}(x,y,z)\right) \Big/ CI_{max,min}(x,y,z) \quad (4.4)$$

and assigned to the voxel, creating volumes of percent change in attenuation coefficient while maintaining the spatial specificity of μ in the cortical tissue (See Appendix A5). As a result, time points where the mean attenuation value was within the C.I. for a given voxel are made visually distinct from those that were statistically significantly above (red) or below (blue) this normative range.

4.3. Results

4.3.1. Global and focal control results

Using the method described in Section 4.2.3, attenuation coefficient volumes were calculated from the intensity volumes for all of the global and focal control and seizure experiments. 0.5 x 0.5 x 0.5 mm ROI were selected in regions outlined in Chapter 3 and Figure 4.2 shows the percent change in average attenuation values for both the global (Figure 4.2A) and the focal (Figure 4.2B) control experiments. The 2SDs of the baseline means were ±2.5% for the global model and ±2% for the focal model, plotted as red, horizontal, dashed lines in Figure 4.2, indicating the intrinsic fluctuation in the

attenuation values with time. The percent change in attenuation stayed within the 2SD throughout the control experiments for both models.

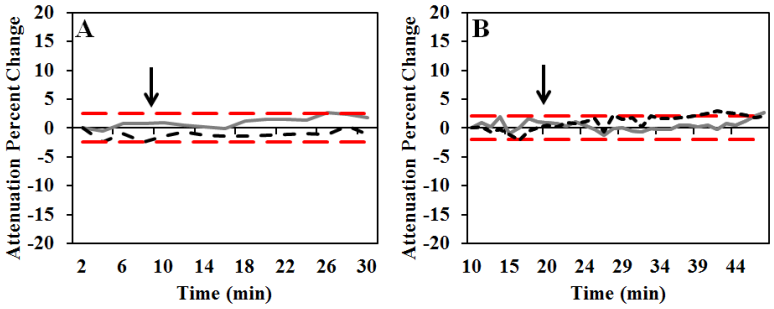

Figure 4.2 Percent change in average attenuation for (A) Global and (B) Focal controls 0.5 x 0.5 x 0.5 mm ROIs. Global ROIs are separated 1 mm laterally. Focal ROIs are located at the injection site (solid gray) and 2 mm from the injection site (dashed black). Arrows represent time of injection. Red horizontal bars: 2SD of the baseline mean.

4.3.2. Changes in attenuation during global and focal seizures

Using the global and focal *in vivo* seizure intensity volumetric data previously analyzed in Chapter 3, we calculated depth-resolved attenuation coefficient volumes and the C.I. statistical analysis was performed for visualization and localization of changes in attenuation coefficient during seizure.

Figure 4.3 and Figure 4.4 show the total count of attenuation values in three different layers of the cortical tissue: layer A was the top 65 μm under the surface, layer B was the following 52 μm, and layer C was the following 130 μm. Layer thicknesses were determined based on visual inspection of Δμ patterns visible in the *f*OCT volumes in Figure 4.5 and Figure 4.6. The left graphs are the baseline distribution of attenuation values and the right graphs are the post seizure distribution of attenuation values.

When conducting the global seizure experiments, five volumes were acquired prior to PTZ injection providing a *df* of four, allowing for the use of a 0.95 confidence

level. The black line outlined on the histograms in Figure 4.3 represents the binned counts of attenuation coefficient values within the calculated 0.95 confidence level for each of the three distinct layers. From these parameters and the five baseline volumes, a C.I. for each 30 x 30 x 30 μm voxel was calculated using the method described in Section 4.2.4.

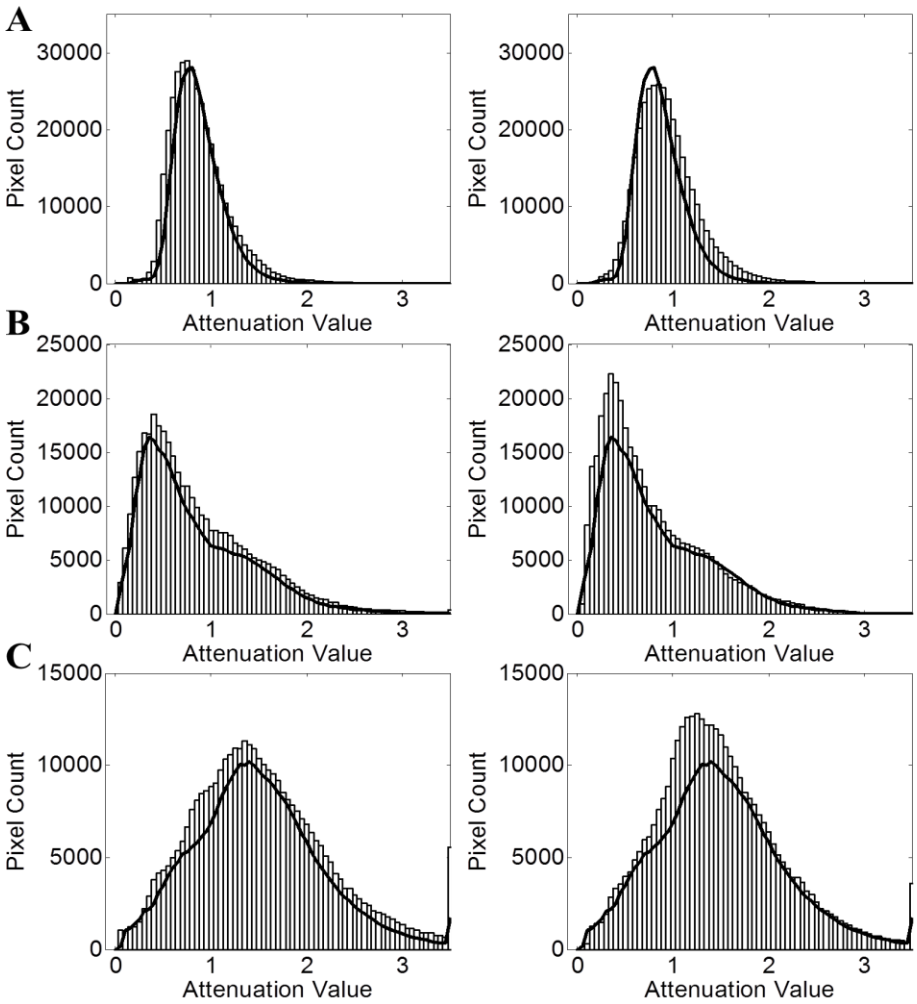

Figure 4.3 Histograms of the attenuation value distribution in three layers of the cortical tissue in a global model experiment for baseline (Left) and post seizure onset (Right). The black line is the baseline attenuation values that formed the 0.95 confidence level. Layer (A) top 65 μm, layer (B) following 52 μm, and layer (C) following 130 μm.

For the first set of focal experiments (3 x 3 x 2 mm volumes), the C.I. formation, as seen in Figure 4.4, was similar to the global experiments except only three volumes, which were acquired post 4-AP injections but prior to seizure onset, were used to form the baseline dataset. Due to the fact that this provided a *df* of only two, the use of a 0.90 confidence level was required. Tissue deformation resulting from the injections inhibited the use of earlier volumes. The left graphs in (Figure 4.4) are the baseline distribution of attenuation values and the right graphs are the post seizure distribution with each layer's 0.90 confidence level displayed as the black line.

When comparing the distribution changes in attenuation values between baseline and post seizure as well as between global and focal seizure models, it is apparent that in the focal model there is a distinct difference between the three layers. The distribution of the top layer (Figure 4.4A) shifts to the right post seizure, indicating a significant increase in the attenuation values while the middle layer (Figure 4.4B) shows very little shift and the bottom layer (Figure 4.4C) shows a large shift to the left indicating a significant decrease in the attenuation values. In the focal seizure there is a layer dependent change in attenuation where the global model (Figure 4.3) shows significant deviations from the defined confidence level line, but no layer dependent directionality to the changes.

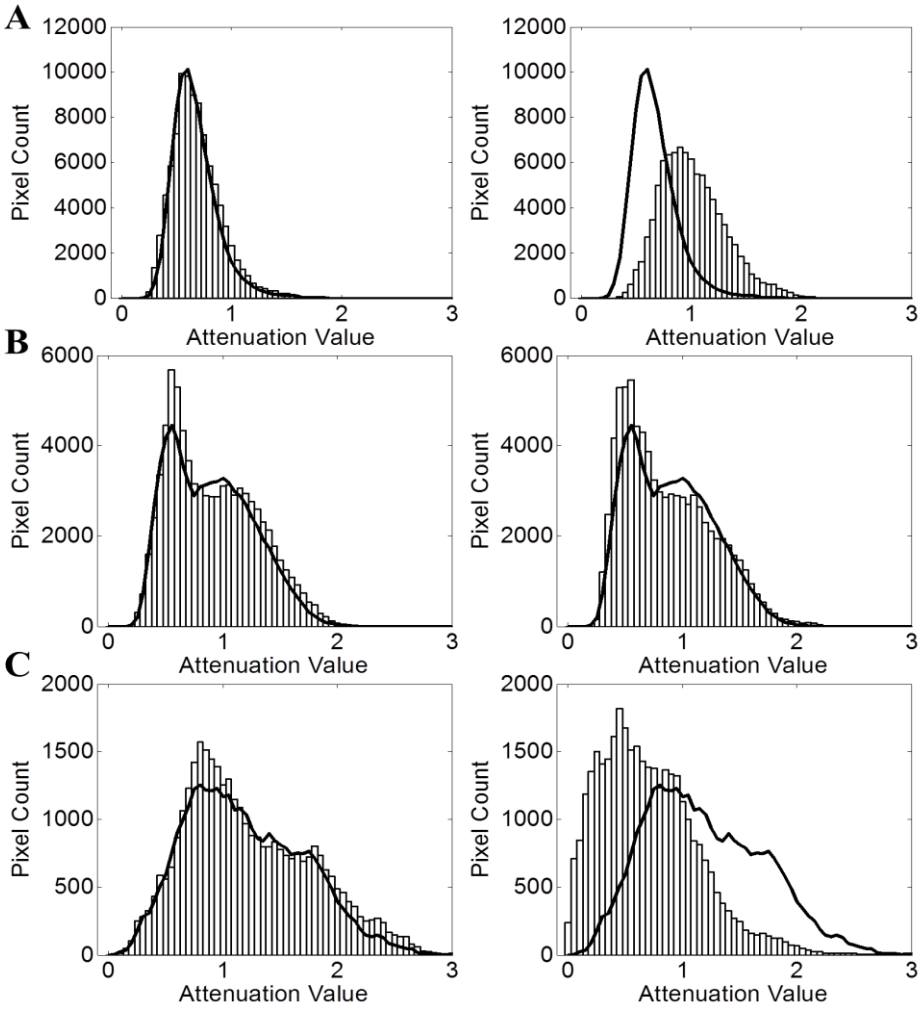

Figure 4.4 Histograms of the attenuation value distribution in three layers of the cortical tissue in a focal model experiment for baseline (Left) and post seizure onset (Right). The black line is the baseline attenuation values that formed the 0.90 confidence level. Layer (A) top 65 μm, layer (B) following 52 μm, and layer (C) following 130 μm.

4.3.3. Visualization of fOCT volumes for global and focal seizure progression

In order to visualize the spatial distribution of the changes in attenuation coefficient for both the global and focal seizure models, 3D *f*OCT volumes [52,54,57,58] were created. As defined in Section 4.2.4, for each voxel in every volume post baseline, a Δμ above or below the C.I. was calculated and then each voxel was assigned a color ranging from black to color saturation, at a maximum percent change threshold, with gradations of red

representing voxels of percent change above the C.I. and gradations of blue representing voxels of percent change below the C.I.

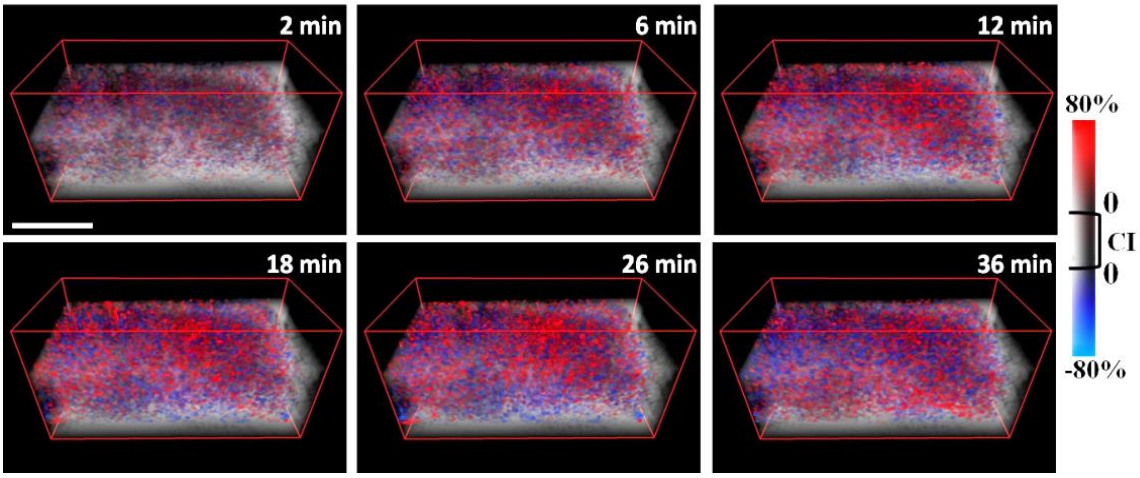

Figure 4.5 *f*OCT volumes of the global seizure 4 x 2 x 2 mm. Color is scaled from black to color saturation at -80% Δμ for blue and 80% Δμ for red representing decreased and increased Δμ respectively. *f*OCT volumes are combined with corresponding attenuation coefficient volumes. Time is min post PTZ injection. Top of image: Bregma, left of image: Rostral. Bar: 1 mm.

Figure 4.5 *fOCT* volumes of the global seizure 4 x 2 x 2 mm. Color is scaled from black to color saturation at -80% Δμ for blue and 80% Δμ for red representing decreased and increased Δμ respectively. *fOCT* volumes are combined with corresponding attenuation coefficient volumes. Time is min post PTZ injection. Top of image: Bregma, left of image: Rostral. Bar: 1 mm. shows the global seizure *f*OCT volumes numbered as minutes post PTZ injection with Δμ saturating at ± 80% for both red and blue voxels. We combined the *f*OCT volumes with their corresponding attenuation coefficient volumes to show the precise anatomical registration of the *f*OCT volumes as well as provide a reference to the location of Δμ in the cortical tissue. In the global model, voxels that exhibit both positive and negative Δμ are distributed throughout the imaged tissue. Significant changes in Δμ begin to accumulate throughout the tissue 6 min post PTZ injection and continue through full seizure (24 min), saturating

at ± 80% Δμ (Figure 4.5). The *f*OCT volumes maintain the spatial distribution of the voxels and eliminate the need for averaging, providing voxel specific Δμ and revealing significant percent changes in attenuation as well as the heterogeneous distribution of both positive and negative Δμ, reflecting the known global nature of seizure progression in the global model.

For the first set of focal model experiments, we acquired 3 x 3 x 2 mm volumes directly at the injection site for optimal spatial resolution during seizure propagation. The resulting *f*OCT volumes are shown in Figure 4.6. Each volume is combined with a corresponding attenuation coefficient volume and Δμ is displayed with saturated blue and red voxels at -50% Δμ and 80% Δμ respectively. We extended the red threshold further than the blue to better visualize the distribution of Δμ since the range of positive percent change in attenuation was larger than the negative. *f*OCT volumes provide visualization of depth-dependent changes in attenuation coefficient and the focal nature of the change in tissue attenuation is illustrated in Figure 4.6. At the surface of the cortical tissue, a significant increase in Δμ is visible starting at 16 min, which corresponds with seizure onset displayed as the increase in electrical activity detected by the implanted electrode. The increase in Δμ begins to coalesce starting at 20 min post-4-AP injections. Directly below, there is a corresponding region where Δμ significantly decreases through focal seizure onset, initiating 24 min post 4-AP injections (Figure 4.6). To further quantify the depth-dependent regions exhibiting differing changes in attenuation coefficient, we averaged the Δμ in three small ROIs (0.2 x 0.2 x 0.2 mm), which were stacked in depth

and plotted versus time for all three regions (Figure 4.7). The top ROI exhibited positive Δμ, the middle ROI exhibiting no Δμ, and the bottom ROI exhibiting negative Δμ.

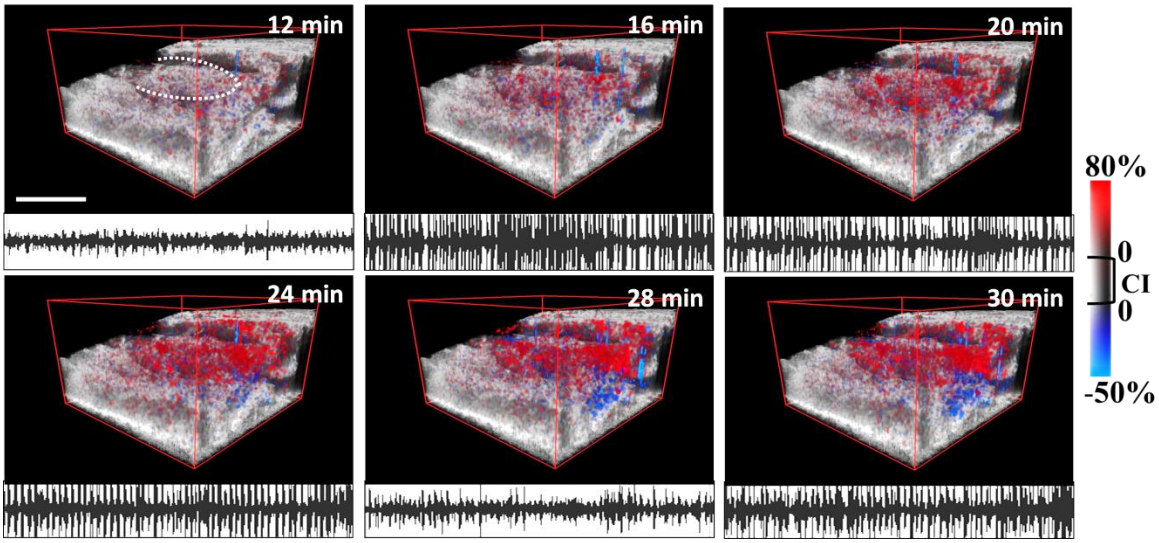

Figure 4.6 *f*OCT volumes of the focal seizure 3 x 3 x 2 mm 1 min electrical trace ±1 mV displayed below. Color is scaled from black to color saturation at -50% Δμ for blue and 80% Δμ for red representing decreased and increased Δμ respectively. *f*OCT volumes are combined with corresponding attenuation volumes. Time is min post 4-AP injections. Left-back of image: Rostral, right-back of image: Bregma. Dashed line in first frame indicates location of injection pipette. Bar: 1 mm.

The plot in Figure 4.7 shows the average Δμ as a function of time post 4-AP injections in each of the ROIs. The top ROI shows an increase of 15% by the end of the focal seizure (30 min post 4-AP injections) and a significant change as early as 14 min post injections. The middle ROI shows no significant Δμ through focal seizure onset. The bottom ROI shows a decreasing trend, but does not reach a maximum change of -11% until 30 min post 4-AP injections and the change does not become significant until 16 min after the top ROI. The *f*OCT volumes enable the localization of changes in attenuation coefficient of seizing tissue as well as the differentiation between localized regions of cortical tissue exhibiting different spatial and temporal changes in attenuation coefficients during seizure progression.

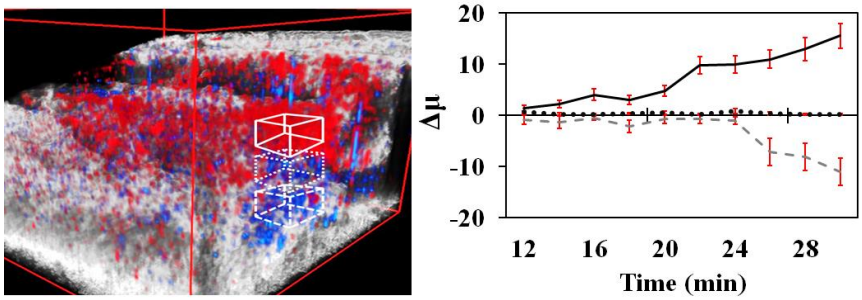

Figure 4.7 *f*OCT volume 30 min. post 4-AP injections showing 0.2 x 0.2 x 0.2 mm ROIs for three regions exhibiting increasing (solid), no change (dotted), and decreasing (dashed) Δμ plotted vs. time through focal seizure progression. Error bars are standard error.

4.3.4. Focal seizure spatiotemporal propagation

Once we verified that we could detect changes in attenuation coefficient locally during a focal seizure, we expanded our imaging field of view to determine if we could visualize how focal seizures propagate from the injection site. To maintain reasonable temporal resolution while increasing the field of view, single volumes of 150 images composed of 512 A-lines were acquired every 40 s. We acquired 5 x 4 x 2 mm volumes with five volumes, acquired prior to the last 4-AP injection. Five baseline volumes providing a *df* of four, allowed for the use of a 0.95 confidence level. The Δμ values were calculated for each volume from which *f*OCT volumes were generated with both blue (negative Δμ) and red (positive Δμ) saturating at ±30% (Figure 4.8). The 4-AP injections were administered 1 mm from the right edge of the volume and 2 mm from bregma with the pipette tip outlined in the first fame in Figure 4.8. From the *f*OCT volumes, we were able to identify localized regions that exhibit both positive and negative change in attenuation as well as the spatial propagation from the injection site.

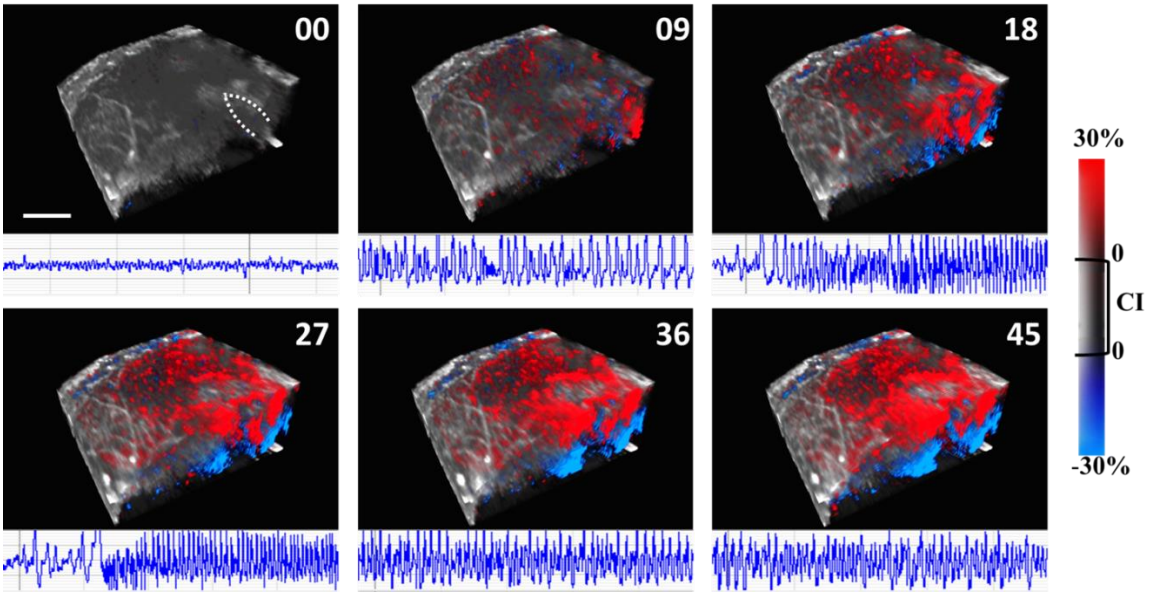

Figure 4.8 *f*OCT volumes of focal seizure 5 x 4 x 2 mm with their corresponding 30 s electrical trace ±1 mV displayed below. Color is scaled from black to color saturation at -30% Δμ for blue and 30% Δμ for red representing decreased and increased Δμ respectively. *f*OCT volumes are combined with corresponding attenuation volumes. Time is min post 4-AP injections. Dashed line in frame one indicates location of injection pipette. Right back of image: Bregma, front of image: Rostral. Scale bar: 1 mm.

As a representative of the results for the focal seizure experiments, Figure 4.8 shows the *f*OCT volumes minutes post 4-AP injections. Significant changes in attenuation begin 9 min post injection and correspond with the onset of electrical seizure activity recorded at the site of injection from the implanted electrode, shown as the 30 min electrical trace below each frame. The changes in attenuation coefficient begin to coalesce at the injection site 18 min post injections and continue to propagate radially as the focal seizure progresses resulting in a 1 mm area with maximum change. The results from these experiments also show the layering pattern of changes in attenuation seen previously. We further investigated the layers of cortical tissue showing differing trends in attenuation changes by analyzing them as three distinct layers in time post 4-AP injection (Figure 4.9). Layer A was the top 65 μm under the surface, Layer B was the

following 52 µm, and Layer C was the following 130 µm and the widths of the layers were selected based on the spatial Δµ patterns observed in the *f*OCT volumes *a posteriori*. Figure 4.9 shows the *f*OCT data in each of the three layers in time post 4-AP injections as maximum intensity projections (MIPs), which were calculated by collapsing the *z*-axis of each layer in each volume into a 2D *en face* image representing the largest positive or negative Δµ in depth at each pixel. The colors span from white to color saturation at ±30%.

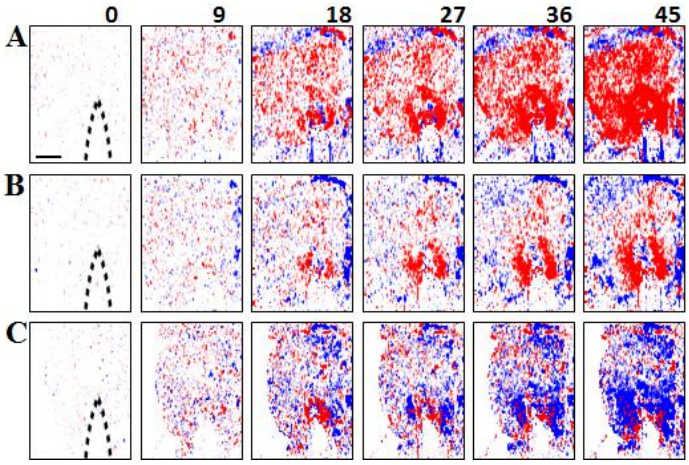

Figure 4.9 MIP layered *f*OCT data minutes post 4-AP injections. Layer (A) top 65 µm, layer (B) following 52 µm, and layer (C) following 130 µm. Dashed line in frame one of each layer indicates location of injection pipette. Color spans from white to color saturation at ±30% Bar: 1mm.

We further investigated the spatiotemporal propagation of the attenuation changes by selecting 0.5 x 0.5 mm ROIs with three consecutively in front of and three consecutively lateral of the injection site (Figure 4.10(a-f)). Due to the placement of the pipette with respect to the midline bone, 3 mm of the brain tissue with a hemicraniectomy was to the left of the injection pipette and thus a lateral progression of small ROIs were analyzed in this same direction. We kept the same three layer thicknesses (A, B, and C) and plotted the average Δµ from each of the ROIs as red, black, and blue lines

respectively over time post 4-AP injections. In both ROIs (a) and (d) in Figure 4.10 there are significant changes in Δμ in layer A and C with a 30-60% increase and a 15-30% decreases during focal seizure propagation. Similarly to the earlier described 4-AP experiments, the decreasing lower layer C did not exhibit a significant change until minutes after the increasing trend. A -5% decrease occurred 34 min post injection, 10 min after a 5% increase in ROI (a). Similarly there is an 8 min delay between the 5% increase and the -5% decrease in ROI (d). Unlike the earlier described 4-AP experiments, however, significant changes also occurred in layer B in some regions (Figure 4.10d) and followed a similar pattern as layer A except with a more limited propagation radius. As the ROIs step forward and lateral from the injection site, the average Δμ values begin to decrease as seen in the plots in (Figure 4.10 b-c and e-f) where a maximum of only 10-15% increase and -5-10% decrease occurred with some layers not even exhibiting a greater than ±1% change.

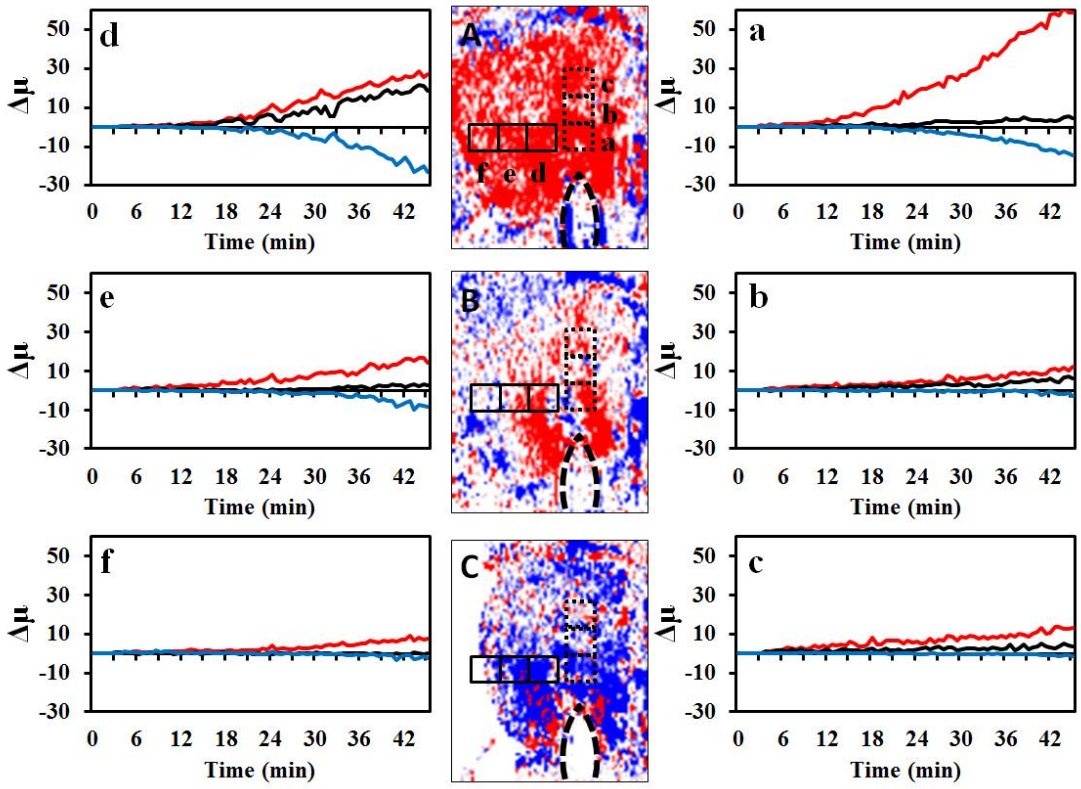

Figure 4.10 Consecutive ROIs of average Δμ in front of and lateral of the site of 4-AP injections. Six 0.5 x 0.5 mm ROIs (a-f) were averaged for three layers (A-C). The letter next to the ROI in the top frame refers to the plot with the corresponding letter plotted vs. time post 4-AP injections. Layer A (Red line in plots): top 65 µm, layer B (Black line in plots): following 52 µm, and layer C (Blue line in plots): following 130 µm. Dashed line on each layer indicate location of pipette. MIPs are of the *f*OCT volume 45 min post injections.

4.4. Discussion

In order to better understand the optical properties of the cortical tissue during seizures independent from system intensity levels, we generated volumes of depth-resolved attenuation coefficient values. Previous research observed a depth-dependence to the changes in scattering during neural activation [52,54,56,58] and depth-resolved attenuation coefficient volumes provided an even further understanding of the optical properties of cortical tissue by incorporating changes in both absorption and scattering coefficients. The development of the *f*OCT volumes provided high resolution tracking of

the spatiotemporal changes of the tissue attenuation values as both global and focal seizures propagate through cortical tissue *in vivo*. In the global seizure model, the *f*OCT volumes revealed significant percent changes in attenuation as well as the heterogeneous distribution of both positive and negative $\Delta\mu$, reflecting the known global nature of seizure progression in the global model. In the focal seizure model *f*OCT volumes, distinct depth-dependent regions exhibiting differing changes in attenuation coefficient were observed. From the analysis of $\Delta\mu$, we were able to clearly differentiate between a global (PTZ) seizure model and focal (4-AP) seizure model and further investigations are necessary to determine the underlying mechanisms that elicited the changes in attenuation during pathologic levels of neural activity.

4.5. Conclusion

To utilize the spatiotemporal resolution provided by OCT, we developed an analytical method, creating *f*OCT volumes, to display statistically significant changes in the attenuation coefficient of cortical tissue while maintaining high spatial specificity. We were able to differentiate between global and focal seizures through the spatiotemporal pattern of $\Delta\mu$. In the global model, there was a large change in attenuation throughout the tissue, where in the focal model, only a localized region around the injection site showed significant changes in attenuation. The voxel values, which incorporated 30 x 30 x 30 μm of tissue, provided localized visualization of the changes in attenuation coefficient during seizure progression. Through the inclusion of implanted electrodes in our focal model, we were able to verify that the electrical detection of seizure onset corresponds temporally to significant changes in attenuation. In addition, we were able to quantify depth-resolved

changes in attenuation and track focal seizure propagation with high spatiotemporal resolution. The results from this study demonstrate the potential utility of OCT as a minimally-invasive tool for studying seizure onset and propagation with high spatiotemporal resolution.

Chapter 5. Investigating the Biological Mechanisms Eliciting the Attenuation Changes During Seizures

5.1. Introduction

A variety of optical imaging techniques such as IOS imaging [37,38,41,42,77] and NIR spectroscopy [46,65,78] have been used to investigate the multiple optical changes resulting from biological events that occur in tissue during neurological and seizure activity. These events, such as cellular swelling, changes in the ECS, and the changes in the cerebral blood volume (CBV) and hemodynamics [16,66,79,80] affect both the scattering and absorption of light within tissue and it can be difficult to clearly attribute a particular biological changes with the resulting optical changes.

In order to further ascertain what biological mechanisms are eliciting the attenuation coefficient changes during the seizures observed in Chapter 3 and 4, we first utilized phase-resolved Doppler OCT in order to differentiate between changes in attenuation within large blood vessels vs. changes in tissue minus major blood vessels. We performed Doppler processing on the *in vivo* focal seizure imaging data collected during the experiments outlines in Chapter 4 [76]. Second, we conducted *in vitro* seizure experiments to look at changes in attenuation values in cortical slices independent of the effect from blood.

5.2. Materials and experimental methods

5.2.1. Brain slice preparation for experimentation with an MEA

We use JAX C57/BL6 wild type mice between postnatal day (P) 15 to P25 of either sex. Mice are anesthetized with isoflurane, quickly decapitated, and then the brain is rapidly removed and submerged in ice cold dissection solution. 300 μm thick coronal brain slices

are made using a Leica vibrotome in oxygenated ice cold low Ca^{2+}, high Mg^{2+} dissection solution. Slices are then moved to a holding chamber and incubated in oxygenated artificial cerebrospinal fluid (ACSF) at 32 ^{o}C for 1 hr. After the hour, the holding chamber is moved from the incubator to the table top allowing the solution and slices to come to room temperature for 30 mins. Recordings are done on a MultiChannel Systems 60-channel perforated multielectrode array (pMEA). pMEA consists of an 8x8 TiN electrode grid with 200 μm spacing between electrodes and 30 μm electrode diameter. Brain slices are positioned such that the electrode grid is able to record from the entire hippocampus. Local field potential (LFP) recordings from the hippocampus are done under constant ACSF perfusion at ~2 mL/min and at 32 ^{o}C. Epileptiform activity is induced through bath application of 100 μM 4-AP post a 5 min baseline.

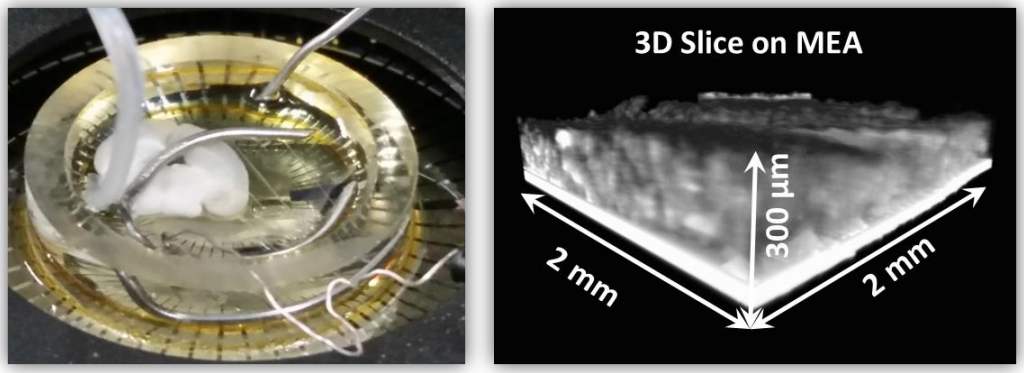

Figure 5.1 (Left) Mouse brain slice with the hippocampus plated on the electrode array. (Right) Volume rendering of the imaged region of the slice composed of 100 attenuation images spanning 2 x 2 mm.

5.2.2. Image acquisition and OCT data processing

For the *in vitro* experiments, volumetric data acquisition was performed with axial depth profiles (A-lines) acquired at 15 kHz. A single volume of 100 sagittal, cross-sectional images composed of 1024 A-lines was acquired every 30 s with an imaging depth of

2 mm. The post processing is described in Chapter 3 and 4 to generate registered 3D attenuation volumes as seen in Figure 5.1 where a 300 μm slice is placed on top of the highly attenuating MEA. 5 min of baseline volumes were collected and for 25 min post 4-AP application through seizure onset.

5.2.3. Phase-resolved Doppler OCT for attenuation analysis

Phase-resolved Doppler analysis was performed on the OCT image data collected during the *in vivo* 4-AP seizure experiments described in Chapter 4. Phase variance volumes were calculated as described in Chapter 1.4 and a blood vessel segmentation algorithm was developed (Figure 5.2) in order to differentiate between changes in attenuation within large blood vessels vs. changes in tissue during seizures. From the phase variance volumes, a 3D mask was calculated to segment the blood vessels in the top 60 μm of cortical tissue. A positive variance mask was created in order to mask only the significant blood flow regions using a threshold of 0.7π, which only allowed for blood vessels with high levels of blood flow (Figure 5.2 top). The mask was then applied to every attenuation volume, segmenting only the attenuation pixels that were within the masked areas. In order to analyze the attenuation changes in pixels not within large blood vessels, in inverse variance mask was created (Figure 5.2 bottom). The threshold in this mask was lowered, however, to 0.5π in order to encompass more of the vascular network, ensuring its removal from the analysis. The inverse mask was then applied to every attenuation volume, creating attenuation volumes minus major blood vessel pixels.

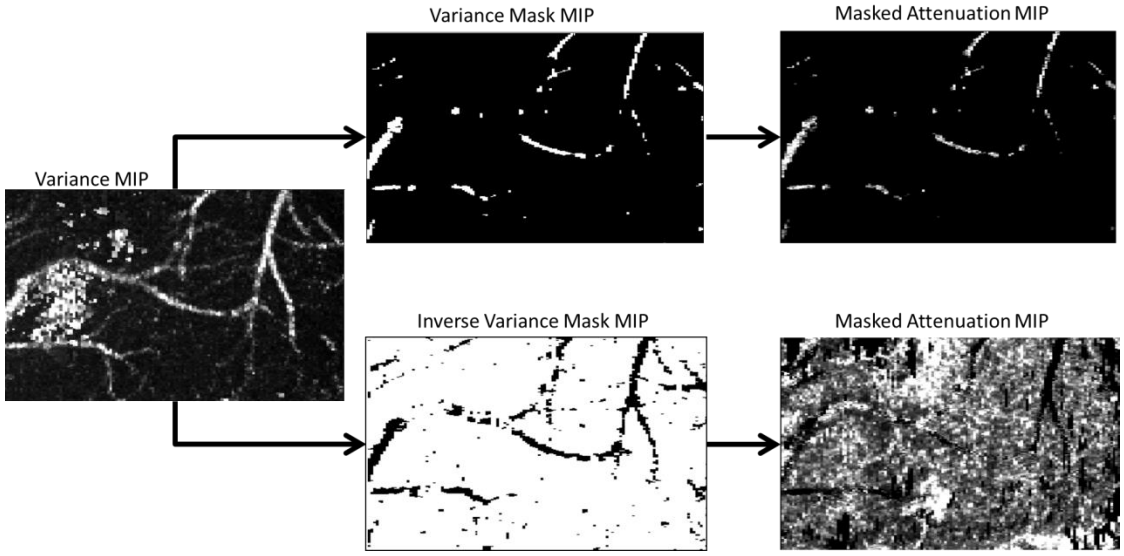

Figure 5.2 Phase variance segmentation algorithm processing diagram. From the variance volumes (top row) a positive mask segmenting out only major blood vessels was created and applied to the attenuation volumes, (bottom row) an inverse variance mask was created to exclude blood vessels and applied to the attenuation volumes. All images are maximum intensity projections (MIP) of the top 60 μm of cortical tissue from the *in vivo* 4-AP experimental data in Chapter 4.

5.3. Results

5.3.1. Contribution of changes in hemodynamics and blood flow in attenuation changes

In order to differentiate between changes in attenuation within large blood vessels vs. changes in tissue without the contribution of blood vessels during seizures, we analyzed the resulting segmented attenuation volumes. The average attenuation values were calculated for each volume and plotted in time minutes post 4-AP injections (Figure 5.3). The black dashed line represents the average attenuation coefficient values within the blood vessels and the red line represents the average attenuation coefficient values in the cortical tissue minus major blood vessel pixels (Figure 5.3).

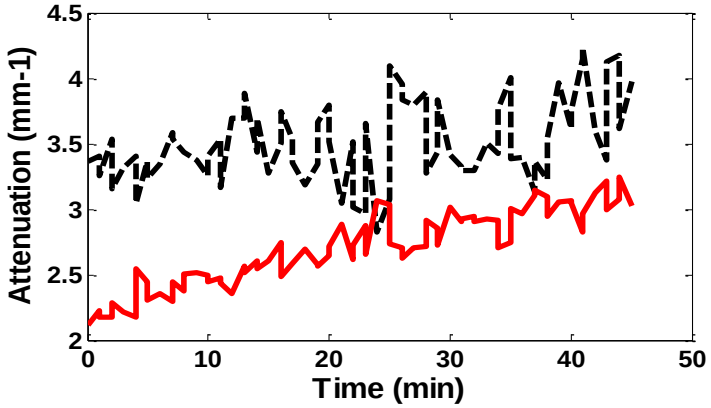

Figure 5.3 Average attenuation coefficients plotted vs. time min post 4-AP injections. Black dashed line: avg. attenuation within blood vessels, Red line: avg, attenuation in the cortical tissue without blood vessels.

5.3.2. Attenuation changes during in vitro 4-AP activation

To analyze the changes in attenuation coefficient during the *in vitro* 4-AP seizure experiments, we calculated the average attenuation from 1.5 x 0.5 x 0.2 mm ROIs within our volumetric data, which was acquired over the hippocampal region of the brain slice. Figure 5.4 shows the results from two experiments of the percent change in the average attenuation coefficient (Δμ) plotted vs. time along with the ±2SD above and below the baseline mean for the extent of the experiment.

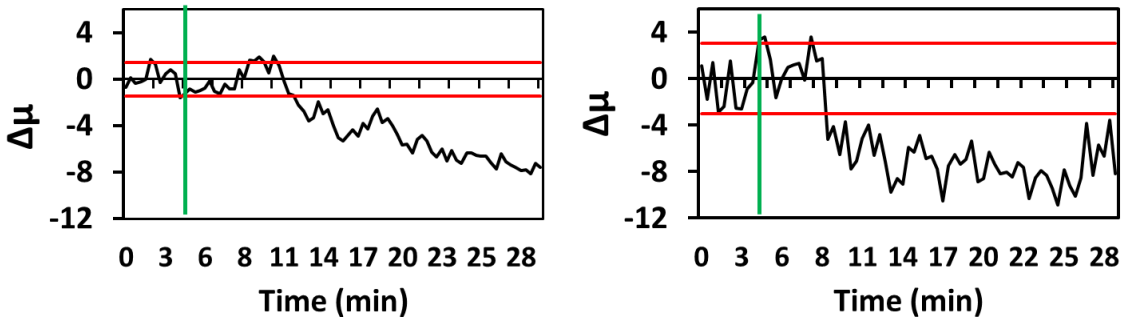

Figure 5.4 Percent change in average attenuation coefficient vs. time (min) from 1.5 x 0.5 x 0.2 mm ROIs within the volumetric data. Green line: application of 4-AP, Red lines: ±2SD interval above and below the mean of the 5 min baseline values.

An advantage of our *in vitro* model was the ability, through the use of an MEA, to non-invasively detect the electrical activity from across the entire hippocampal region of the

brain slice. Figure 5.5 shows one of the experimental results from Figure 5.4 with its corresponding electrical trace from a representative activated electrode on the MEA plotted in time. This provides direct spatiotemporal comparison of the optical and electrical changes and 3D attenuation coefficient changes can be compared with the sequence of *f*OCT volumes (Figure 5.5).

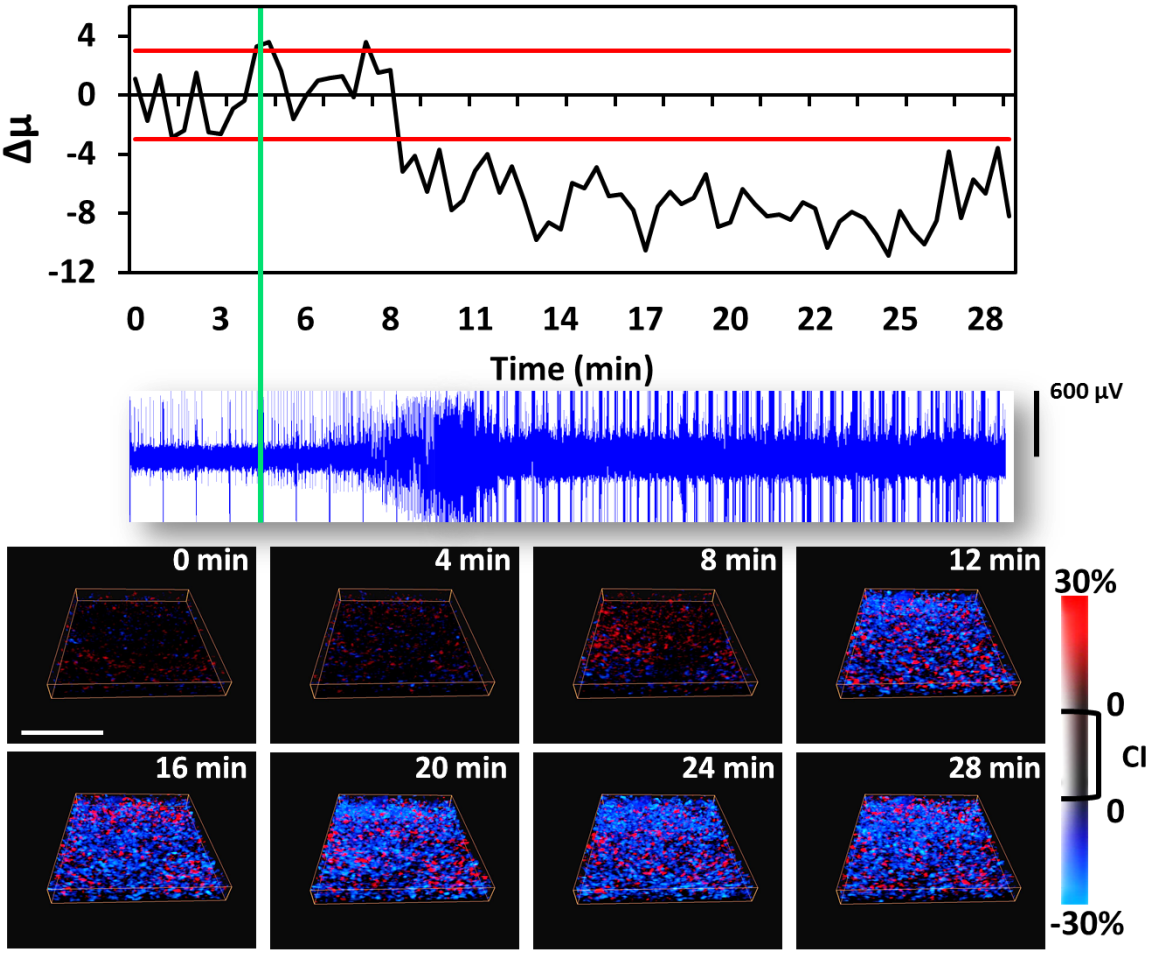

Figure 5.5 Percent change of attenuation coefficient plot from Figure 5.4 and a representative electrical trace from an MEA electrode plotted vs. time (min). *f*OCT Δμ volumes 2 x 2 mm, 200μm thick cortical slice. Color is scaled from black to color saturation at -30% Δμ for blue and 30% Δμ for red representing decreased and increased Δμ respectively. Scale bar: 1mm

5.4. Discussion

Our goal was to ascertain what the biological processes are that elicited the attenuation changes during the seizure activity we observed *in vivo* with OCT. To achieve this, we first utilized phase-resolved Doppler OCT in order to differentiate between changes in attenuation within large blood vessels vs. changes in tissue minus major blood vessels. The results in Figure 5.3 show that the attenuation values within the blood vessels stays within 3 - 4 mm^{-1} during the extent of the experiment. However, the attenuation values that exclude the major blood vessels start at values close to 2 mm^{-1}, but increase to 3 mm^{-1} during seizure progression, which is within the range of attenuation coefficients values within the blood vessels. These results indicate that during seizure there is an increase in the CBV in the cortical tissue, most likely through the capillary network, which our Doppler analysis does not include, resulting in the increase in attenuation in that region to values observed for blood alone. These results correspond well with the attenuation trends found in Chapter 4.3.3 in the upper layer ROI, allowing us to assume that the increasing in attenuation coefficient is due to an increase in the CBV and hemodynamic changes during seizures.

The second approach we took to further understand the attenuation changes we see during seizures was to conduct a new set of seizure experiments. This time, however, we conducted *in vitro* experiments on cortical brain slices, removing the blood flow dynamics as a contributing factor to the attenuation changes. Figure 5.4 and Figure 5.5 show representative results from these experiments, where we observed significant decreases in the percent change of average attenuation coefficients during the onset of

seizure. There was an 8 - 10% decrease in attenuation during the experiments and this corresponds well with the percent decreases we observed *in vivo,* outlined in Chapter 4.3.4, which tended to be smaller than the percent increases. In addition, the percent change became significant 5 - 8 min post 4-AP application, which is faster than *in vivo,* but the temporal dynamics are probably different between *in vivo* and *in vitro* 4-AP seizure models especially due to the use of anesthesia in our *in vivo* model. The timing in which the decrease in attenuation became significant corresponded well with seizure onset indicated by the Epileptiform activity recorded from the MEA, verifying the presence of seizure throughout the hippocampus.

From these results, we can conclude that there are changes in attenuation during seizures that are independent from change in CBV and hemodynamic changes. The fact that the attenuation trends correspond well with results found in other reflective imaging techniques during neurological and seizure activation of cortical tissue indicated the decreasing trends are linked to changes due to cellular swelling and changes in the ECS volume [37,39,41–43,54,66,77].

5.5. Conclusion

In conclusion, we previously identified differing trends in attenuation coefficient changes during seizure onset (Chapter 4). We utilized two methods in order to further ascertain what biological mechanisms are eliciting these changes. We first used phase-resolved Doppler OCT in order to segment the cortical tissue into blood vessels and no blood vessels. When we analyzed the attenuation coefficient changes in each of these areas during seizure, we observed an increase in attenuation, in the region without blood

vessels, to the coefficient values observed within the blood vessels, concluding the changes in attenuation coefficients in the upper layers of the cortical tissue are due to increase in CBV through the capillary network. The second method, we conducted *in vitro* seizure experiments to remove the effect of blood flow on the changes in attenuation coefficient. From these experiments, we observed a significant percent decrease in attenuation throughout the hippocampus and that the decrease in attenuation corresponded well with the onset of seizure indicated by the Epileptiform activity recorded from the MEA. From these results, we can conclude that there are changes in attenuation during seizures that are independent from change in CBV and the hemodynamic effects, but are linked to changes in cellular swelling and the ECS volume.

Bibliography:

1. E. M. C. Hillman, "Optical brain imaging in vivo: techniques and applications from animal to man," J. Biomed. Opt. **12**, 1–49 (2007).
2. D. N. Lenkov, A. B. Volnova, A. R. D. Pope, and V. Tsytsarev, "Advantages and limitations of brain imaging methods in the research of absence epilepsy in humans and animal models.," J. Neurosci. Methods **212**, 195–202 (2013).
3. M. Choma, M. Sarunic, C. Yang, and J. Izatt, "Sensitivity advantage of swept source and Fourier domain optical coherence tomography.," Opt. Express **11**, 2183–9 (2003).
4. J. F. de Boer, B. Cense, B. H. Park, M. C. Pierce, G. J. Tearney, and B. E. Bouma, "Improved signal-to-noise ratio in spectral-domain compared with time-domain optical coherence tomography.," Opt. Lett. **28**, 2067–9 (2003).
5. D. Huang, E. A. Swanson, C. P. Lin, J. S. Schuman, W. G. Stinson, W. Chang, M. R. Hee, T. Flotte, K. Gregory, C. A. Puliafito, and J. G. Fujimoto, "Optical Cohernece Tomography," Science (80-.). **254**, 1178–1181 (1991).
6. R. Leitgeb, W. Drexler, A. Unterhuber, B. Hermann, T. Bajraszewski, T. Le, A. Stingl, and A. Fercher, "Ultrahigh resolution Fourier domain optical coherence tomography.," Opt. Express **12**, 2156–65 (2004).
7. B. H. Park, M. C. Pierce, B. Cense, S. Yun, M. Mujat, G. J. Tearney, B. E. Bouma, and J. F. De Boer, "Real-time fiber-based mulit-functional sepctral-domain optical coherence tomography at 1.3 μm," Opt. Express **13**, 3931–3944 (2005).
8. J. M. Schmitt, "Optical coherence tomography (OCT): a review," IEEE J. Sel. Top. Quantum Electron. **5**, 1205–1215 (1999).
9. S. Yun, G. Tearney, B. Bouma, B. Park, and J. de Boer, "High-speed spectral-domain optical coherence tomography at 1.3 mum wavelength.," Opt. Express **11**, 3598–604 (2003).
10. J. Fujimoto, C. Pitris, S. Boppart, and M. Brezinski, "Optical Coherence Tomography: An Emerging Technology for Biomedical Imaging and Optical Biopsy," Neoplasia **2**, 9–25 (2000).
11. M. R. Hee, J. A. Izatt, E. A. Swanson, D. Huang, J. S. Schuman, C. P. Lin, C. A. Puliafito, and J. G. Fujimoto, "Optical Coherence Tomography of the Human Retina," Arch Ophthalmol **113**, 325–32 (2012).
12. C. Catana, A. Drzezga, W.-D. Heiss, and B. R. Rosen, "PET/MRI for Neurological Applications," J. Nucl Med. **53**, 1–22 (2013).
13. M. A. Franceschini, H. Radhakrishnan, K. Thakur, W. Wu, S. Ruvinskaya, S. Carp, and D. A. Boas, "The effect of different anesthetics on neurovascular coupling," Neuroimage **51**, 1367–1377 (2010).
14. A. M. Mishra, H. Bai, A. Gribizis, and H. Blumenfeld, "Neuroimaging biomarkers of epileptogenesis," Neurosci. Lett. **497**, 194–204 (2011).
15. W. W. Moses, "Fundamental Limits of Spatial Resolution in PET," Nucl. instruments methods Phys. Res. **648 Supple**, S236–S240 (2011).
16. H. L. Sloan, V. C. Austin, A. M. Blamire, J. W. H. Schnupp, a. S. Lowe, K. A. Allers, P. M. Matthews, and N. R. Sibson, "Regional differences in neurovascular

coupling in rat brain as determined by fMRI and electrophysiology," Neuroimage **53**, 399–411 (2010).
17. Y. Tai and P. Piccini, "Applications of positron emission tomography (PET) in neurology," J. Neurol. Neurosurg. Psychiatry **75**, 669–676 (2004).
18. T. Tsurugizawa, L. Ciobanu, and D. Le Bihan, "Water diffusion in brain cortex closely tracks underlying neuronal activity," 1–6 (2013).
19. E. Macé, G. Montaldo, I. Cohen, M. Baulac, M. Fink, and M. Tanter, "Functional ultrasound imaging of the brain.," Nat. Methods **8**, 662–4 (2011).
20. J. Fujimoto and W. Drexler, "Introduction to Optical Coherence Tomography," in *Optical Coherence Tomography* (2008), pp. 1–45.
21. J. Izatt and M. Choma, "Theory of optical coherence tomography," Opt. Coherence Tomogr. - Technol. Appl. 47–72 (2008).
22. S. A. Boppart, B. E. Bouma, M. E. Brezinski, G. J. Tearney, and J. G. Fujimoto, "Imaging developing neural morphology using optical coherence tomography," J. Neurosci. Methods **70**, 65–72 (1996).
23. A. M. Rollins, M. D. Kulkarni, S. Yazdanfar, R. Ung-Arunyawee, and J. A. Izatt, "In vivo video rate optical coherence tomography.," Opt. Express **3**, 219–229 (1998).
24. Z. Hu and A. M. Rollins, "Fourier domain optical coherence tomography with a linear-in-wavenumber spectrometer," Opt. Lett. **32**, 3525–27 (2007).
25. N. Nassif, B. Cense, B. Park, M. Pierce, S. Yun, B. Bouma, G. Tearney, T. Chen, and J. de Boer, "In vivo high-resolution video-rate spectral-domain optical coherence tomography of the human retina and optic nerve.," Opt. Express **12**, 367–376 (2004).
26. Y. Wang, C. M. Oh, M. C. Oliveira, M. S. Islam, A. Ortega, and B. H. Park, "GPU accelerated real-time multi-functional spectral-domain optical coherence tomography system at 1300nm," Opt. Express **20**, 14797–813 (2012).
27. K. Bizheva, A. Unterhuber, B. Hermann, B. Povazay, H. Sattmann, W. Drexler, A. Stingl, T. Le, M. Mei, R. Holzwarth, H. a Reitsamer, J. E. Morgan, and A. Cowey, "Imaging ex vivo and in vitro brain morphology in animal models with ultrahigh resolution optical coherence tomography.," J. Biomed. Opt. **9**, 719–24 (2004).
28. M. Mujat, B. H. Park, B. Cense, T. C. Chen, and J. F. de Boer, "Autocalibration of spectral-domain optical coherence tomography spectrometers for in vivo quantitative retinal nerve fiber layer birefringence determination.," J. Biomed. Opt. **12**, 1–6 (2007).
29. J. a Izatt, M. D. Kulkarni, S. Yazdanfar, J. K. Barton, and A. J. Welch, "In vivo bidirectional color Doppler flow imaging of picoliter blood volumes using optical coherence tomography.," Opt. Lett. **22**, 1439–41 (1997).
30. H. Ren, K. M. Brecke, Z. Ding, Y. Zhao, J. S. Nelson, and Z. Chen, "Imaging and quantifying transverse flow velocity with the Doppler bandwidth in a phase-resolved functional optical coherence tomography.," Opt. Lett. **27**, 409–411 (2002).
31. Y. Zhao, Z. Chen, C. Saxer, S. Xiang, J. F. de Boer, and J. S. Nelson, "Phase-resolved optical coherence tomography and optical Doppler tomography for

imaging blood flow in human skin with fast scanning speed and high velocity sensitivity.," Opt. Lett. **25**, 114–116 (2000).
32. V. J. Srinivasan, D. N. Atochin, H. Radhakrishnan, J. Y. Jiang, S. Ruvinskaya, W. Wu, S. Barry, A. E. Cable, C. Ayata, P. L. Huang, and D. A. Boas, "Optical coherence tomography for the quantitative study of cerebrovascular physiology.," J. Cereb. blood flow Metab. **31**, 1339–1345 (2011).
33. B. R. White, M. C. Pierce, N. Nassif, B. Cense, B. H. Park, G. J. Tearney, B. E. Bouma, T. C. Chen, and J. F. de Boer, "In vivo dynamic human retinal blood flow imaging using ultra-high-speed spectral domain optical coherence tomography," Opt. Express **11**, 3490–3497 (2003).
34. S. A. Boppart, "Optical coherence tomography: technology and applications for neuroimaging.," Psychophysiology **40**, 529–41 (2003).
35. K. Deisseroth, "Optogenetics.," Nat. Methods **8**, 26–29 (2011).
36. L. L. Looger and O. Griesbeck, "Genetically encoded neural activity indicators," Curr. Opin. Neurobiol. **22**, 18–23 (2012).
37. P. G. Aitken, D. Fayuk, G. G. Somjen, and D. A. Turner, "Use of intrinsic optical signals to monitor physiological changes in brain tissue slices.," Methods **18**, 91–103 (1999).
38. S. Bahar, M. Suh, M. Zhao, and T. H. Schwartz, "Intrinsic optical signal imaging of neocortical seizures: the "epileptic dip".," Neuroreport **17**, 499–503 (2006).
39. P. Federico, S. G. Borg, A. G. Salkauskus, and B. A. MacVicar, "Mapping patterns of neuronal activity and seizure propagation by imaging intrinsic optical signals in the isolated whole brain of the guinea-pig.," Neuroscience **58**, 461–80 (1994).
40. D. M. Rector, K. M. Carter, P. L. Volegov, and J. S. George, "Spatio-temporal mapping of rat whisker barrels with fast scattered light signals.," Neuroimage **26**, 619–27 (2005).
41. M. Zhao, J. Nguyen, H. Ma, N. Nishimura, C. B. Schaffer, and T. H. Schwartz, "Preictal and ictal neurovascular and metabolic coupling surrounding a seizure focus.," J. Neurosci. **31**, 13292–13300 (2011).
42. O. W. Witte, H. Niermann, and K. Holthoff, "Cell swelling and ion redistribution assessed with intrinsic optical signals," An. Acad. Bras. Cienc. **73**, 337–350 (2001).
43. M. R. Hajihashemi, T. Zhang, B. K. Ormerod, and H. Jiang, "Non-invasive detection of optical changes elicited by seizure activity using time-series analysis of light scattering images in a rat model of generalized seizure.," J. Neurosci. Methods **227**, 18–28 (2014).
44. J. Yang, T. Zhang, H. Yang, and H. Jiang, "A fast multispectral diffuse optical tomography system for in vivo three-dimensional imaging of seizure dynamics," Appl. Opt. **51**, 3461–3469 (2012).
45. T. Zhang, J. Zhou, R. Jiang, H. Yang, P. R. Carney, and H. Jiang, "Pre-seizure state identified by diffuse optical tomography.," Sci. Rep. **4**, 1–10 (2014).
46. M. A. Franceschini and D. A. Boas, "Noninvasive measurement of neuronal activity with near-infrared optical imaging," Neuroimage **21**, 372–386 (2004).

47. L.-D. Liao, M.-L. Li, H.-Y. Lai, Y.-Y. I. Shih, Y.-C. Lo, S. Tsang, P. C.-P. Chao, C.-T. Lin, F.-S. Jaw, and Y.-Y. Chen, "Imaging brain hemodynamic changes during rat forepaw electrical stimulation using functional photoacoustic microscopy," Neuroimage **52**, 562–570 (2010).
48. V. Tsytsarev, B. Rao, K. I. Maslov, L. Li, and L. V Wang, "Photoacoustic and optical coherence tomography of epilepsy with high temporal and spatial resolution and dual optical contrasts.," J. Neurosci. Methods **216**, 142–5 (2013).
49. X. Wang, Y. Pang, G. Ku, X. Xie, G. Stoica, and L. V Wang, "Noninvasive laser-induced photoacoustic tomography for structural and functional in vivo imaging of the brain," Nat. Biotechnol. **21**, 803–806 (2003).
50. Q. Zhang, Z. Liu, P. R. Carney, Z. Yuan, H. Chen, S. N. Roper, and H. Jiang, "Non-invasive imaging of epileptic seizures in vivo using photoacoustic tomography.," Phys. Med. Biol. **53**, 1921–1931 (2008).
51. J. R. Weber, M. Hsu, A. Lin, D. Lee, C. Owen, D. K. Binder, D. J. Cuccia, A. J. Durkin, and B. J. Tromberg, "Noncontact imaging of seizures using multispectral spatial frequency domain imaging," in *OSA BIOMED* (2010).
52. Y. Chen, A. D. Aguirre, L. Ruvinskaya, A. Devor, D. A. Boas, and J. G. Fujimoto, "Optical coherence tomography (OCT) reveals depth-resolved dynamics during functional brain activation.," J. Neurosci. Methods **178**, 162–73 (2009).
53. M. M. Eberle, C. L. Reynolds, J. I. Szu, Y. Wang, A. M. Hansen, M. S. Hsu, M. S. Islam, D. K. Binder, and B. H. Park, "In vivo detection of cortical optical changes associated with seizure activity with optical coherence tomography.," Biomed. Opt. Express **3**, 2700–6 (2012).
54. B. W. Graf, T. S. Ralston, H. J. Ko, and S. A. Boppart, "Detecting intrinsic scattering changes correlated to neuron action potentials using optical coherence imaging.," Opt. Express **17**, 13447–57 (2009).
55. S. W. Jeon, M. A. Shure, K. B. Baker, D. Huang, A. M. Rollins, A. Chahlavi, and A. R. Rezai, "A feasibility study of optical coherence tomography for guiding deep brain probes.," J. Neurosci. Methods **154**, 96–101 (2006).
56. M. Lazebnik, D. L. Marks, K. Potgieter, R. Gillette, and S. A. Boppart, "Functional optical coherence tomography for detecting neural activity through scattering changes.," Opt. Lett. **28**, 1218–20 (2003).
57. R. U. Maheswari, H. Takaoka, H. Kadono, R. Homma, and M. Tanifuji, "Novel functional imaging technique from brain surface with optical coherence tomography enabling visualization of depth resolved functional structure in vivo," J. Neurosci. Methods **124**, 83–92 (2003).
58. U. M. Rajagopalan and M. Tanifuji, "Functional optical coherence tomography reveals localized layer-specific activations in cat primary visual cortex in vivo.," Opt. Lett. **32**, 2614–6 (2007).
59. M. Sato, D. Nomura, T. Tsunenari, and I. Nishidate, "In vivo rat brain measurements of changes in signal intensity depth profiles as a function of temperature using wide-field optical coherence tomography.," Appl. Opt. **49**, 5686–96 (2010).

60. Y. Satomura, J. Seki, Y. Ooi, T. Yanagida, and A. Seiyama, "In vivo imaging of the rat cerebral microvessels with optical coherence tomography.," Clin. Hemorheol. Microcirc. **31**, 31–40 (2004).
61. J. Lee, V. Srinivasan, H. Radhakrishnan, and D. a. Boas, "Motion correction for phase-resolved dynamic optical coherence tomography imaging of rodent cerebral cortex," Opt. Express **19**, 21258 (2011).
62. D. C. Hesdorffer, G. Logroscino, E. K. . Benn, N. Katri, G. Cascino, and W. A. Hauser, "Estimating risk for developing epilepsy: a population-based study in Rochester, Minnesota," Neurology **76**, 23–27 (2011).
63. R. G. Andrzejak, D. Chicharro, C. E. Elger, and F. Mormann, "Seizure prediction: Any better than chance?," Clin. Neurophysiol. **120**, 1465–1478 (2009).
64. W. Stacey, M. Le Van Quyen, F. Mormann, and A. Schulze-Bonhage, "What is the present-day EEG evidence for a preictal state?," Epilepsy Res. **97**, 243–251 (2011).
65. L. Seungduk, L. Hyun J, I. Changkyun, S. Hyung-Cheul, K. Dalkwon, and K. Beop-Min, "Simultaneous Measurement of Hemodynamic and Neuronal Activities Using Near-infrared Spectroscopy and Single-unit Recording," J. Korean Phys. Soc. **58**, 1697–1702 (2011).
66. D. K. Binder, M. C. Papadopoulos, P. M. Haggie, and A. S. Verkman, "In vivo measurement of brain extracellular space diffusion by cortical surface photobleaching.," J. Neurosci. **24**, 8049–56 (2004).
67. K. Holthoff and O. W. Witte, "Intrinsic optical signals in vitro : A tool to measure alterations in extracellular space with two-dimensional resolution," Brain Res. Bull. **47**, 649–655 (1998).
68. K. F. Rajneesh, A. J. Lin, J. J. Yeh, M. S. Hsu, and D. K. Binder, "Optical Detection of the Pre-Seizure State In-Vivo," J. Neurosurg. Abs. **113**, A422–A423 (2010).
69. A. D. Aguirre, Y. Chen, J. G. Fujimoto, L. Ruvinskaya, A. Devor, and D. A. Boas, "Depth-resolved imaging of functional activation in the rat cerebral cortex using optical coherence tomography.," Opt. Lett. **31**, 3459–61 (2006).
70. J. I. Szu, M. M. Eberle, C. L. Reynolds, M. S. Hsu, Y. Wang, C. M. Oh, M. S. Islam, B. H. Park, and D. K. Binder, "Thinned-skull cortical window technique for in vivo optical coherence tomography imaging.," J. Vis. Exp. e50053 (2012).
71. D. K. Binder, K. Oshio, T. Ma, A. S. Verkman, and G. T. Manley, "Increased seizure threshold in mice lacking aquaporin-4 water channels," Neuroreport **15**, 259–262 (2004).
72. K. Akula, A. Dhir, and S. K. Kulkarni, "Effect of various antiepileptic drugs in a pentylenetetrazol-induced seizure model in mice," Methods Find. Exp. Clin. Pharmacol. **31**, 423–432 (2009).
73. C. L. R. Rodriguez, J. I. Szu, M. M. Eberle, Y. Wang, M. S. Hsu, D. K. Binder, and B. H. Park, "Decreased light attenuation in cerebral cortex during cerebral edema detected using optical coherence tomography," Neurophotonics **1**, 025004–1–7 (2014).

74. M. Zhao, H. Ma, M. Suh, and T. H. Schwartz, "Spatiotemporal dynamics of perfusion and oximetry during ictal discharges in the rat neocortex.," J. Neurosci. **29**, 2814–23 (2009).
75. K. A. Vermeer, J. Mo, J. J. A. Weda, H. G. Lemij, and J. F. de Boer, "Depth-resolved model-based reconstruction of attenuation coefficients in optical coherence tomography.," Biomed. Opt. Express **5**, 322–37 (2013).
76. M. M. Eberle, M. S. Hsu, C. L. Rodriguez, J. I. Szu, M. C. Oliveira, D. K. Binder, and B. H. Park, "Localization of cortical tissue optical changes during seizure activity in vivo with optical coherence tomography," Biomed. Opt. Express **6**, 1812–1827 (2015).
77. R. D. Andrew, C. R. Jarvis, and A. S. Obeidat, "Potential sources of intrinsic optical signals imaged in live brain slices.," Methods **18**, 185–196 (1999).
78. F. Wallois, a Patil, C. Héberlé, and R. Grebe, "EEG-NIRS in epilepsy in children and neonates.," Neurophysiol. Clin. **40**, 281–292 (2010).
79. K. S. Patel, M. Zhao, H. Ma, and T. H. Schwartz, "Imaging pre-ictal hemodynamic changes in neocortical epilepsy," Neurosurg Focus **34**, 1–11 (2013).
80. J. A. Hubbard, M. S. Hsu, T. a. Fiacco, and D. K. Binder, "Glial cell changes in epilepsy: Overview of the clinical problem and therapeutic opportunities," Neurochem. Int. **63**, 638–651 (2013).

Appendix: MATLAB code

A1: Fit for spectrometer dropoff for depth correction curve:

```
2
3       s_dropoff = inline('b(1) + b(2).*(sin(((pi/2).*x))./(((pi/2).*x))).^2.*...
4               exp(-(b(3).^2./(2*log(2)).*((pi/2).*x).^2))','b', 'x');
5
6       [bhatH,residV] = nlinfit(pixelsH,dBH,s_dropoff,[10 10 10]);
```

A2: Three-dimensional cross-correlation function:

```
1   function [nRow, nAline, nFrame, dMax] = crosscorrVolume(pdVolume1, pdVolume2)
2
3
4   pdFFT1 = fftn(pdVolume1);
5   pdFFT2 = fftn(pdVolume2);
6
7   pdCorr = ifftn(pdFFT1.*conj(pdFFT2));
8
9   [rowValues, rowIndex] = max(pdCorr, [], 1);
10  [colValues, colIndex] = max(rowValues);
11  [dMax, imageIndex] = max(colValues);
12
13  nAline = colIndex(1,1,imageIndex);
14  nRow = rowIndex(1,nAline,imageIndex);
15  nFrame = imageIndex;
16
```

A3: Attenuation coefficient function:

```
4   if (bAttenCoeff)
5           if (bSubNoiseFactor && bDC)
6               C_pdI = pdIVolume(:,:,nFileNumber);
7               C_pdI = C_pdI - NoiseFactor;
8               C_pdI = C_pdI .* DCFactor;
9           else
10              C_pdI = pdIVolume(:,:,nFileNumber);
11          end
12          C_pdI=abs(C_pdI);
13          for r = 1:size(C_pdI,1)
14              dFactor = sum(C_pdI(r+1:end,:),1);
15              Argument = 1 + C_pdI(r,:) ./ dFactor;
16               Argument(isnan(Argument)) = 1;
17               Argument(Argument == Inf) = 1;
18              pdMu(r,:) = 1/(2*PixelResolution)*log(Argument);
19          end
20  end
```

A4: CI calculation for either a 90% or 95% confidence level

```
XBar(nRow,nCol,nImage)=mean(S);

if CI_95
    SE95=Alpha95*(std(S,1)/sqrt(NumBaseline));
    CIMax95(nRow,nCol,nImage)=XBar(nRow,nCol,nImage)+SE95;
    CIMin95(nRow,nCol,nImage)=XBar(nRow,nCol,nImage)-SE95;

elseif CI_90
    SE90=Alpha90*(std(S,1)/sqrt(NumBaseline));
    CIMax90(nRow,nCol,nImage)=XBar(nRow,nCol,nImage)+SE90;
    CIMin90(nRow,nCol,nImage)=XBar(nRow,nCol,nImage)-SE90;
end
```

A5: Calculation of percent attenuation coefficient change from CI with color assignment

```
64 -                Avg=mean(S);
65 -                if Avg < CIMin95(nrow,ncol,nSlice)
66 -                    FinalRatio(nrow,ncol,nSlice)=(Avg-CIMin95(nrow,ncol,nSlice))/CIMin95(nrow,ncol,nSlice);
67 -                    FinalRatioAbs(nrow,ncol,nSlice)=abs(FinalRatio(nrow,ncol,nSlice));
68 -                    BlueColor=FinalRatioAbs(nrow,ncol,nSlice)/((Thresholdlow)/256);
69 -                    BlueColor(BlueColor>256)=256;
70 -                    ColorImage(nrow,ncol,1)=256-BlueColor;
71 -                    ColorImage(nrow,ncol,2)=256-BlueColor;
72 -                    ColorImage(nrow,ncol,3)=256;
73
74 -                elseif Avg > CIMax95(nrow,ncol,nSlice)
75 -                    FinalRatio(nrow,ncol,nSlice)=(Avg-CIMax95(nrow,ncol,nSlice))/CIMax95(nrow,ncol,nSlice);
76 -                    FinalRatioAbs(nrow,ncol,nSlice)=abs(FinalRatio(nrow,ncol,nSlice));
77 -                    RedColor=FinalRatioAbs(nrow,ncol,nSlice)/(Thresholdhigh/256);
78 -                    RedColor(RedColor>256)=256;
79 -                    ColorImage(nrow,ncol,1)=256;
80 -                    ColorImage(nrow,ncol,2)=256-RedColor;
81 -                    ColorImage(nrow,ncol,3)=256-RedColor;
82
83 -                else
84 -                    FinalRatio(nrow,ncol,nSlice)=0;
85 -                    ColorImage(nrow,ncol,1)=256;
86 -                    ColorImage(nrow,ncol,2)=256;
87 -                    ColorImage(nrow,ncol,3)=256;
88 -                end
```